A unified model of the thermal history of icy planetesimals: Evolution of their temperature, chemical composition and mechanical properties

SIRONO Sin-iti

February, 1998

Abstract

The present thesis discusses evolution of the temperature, chemical composition, tensile stress and strength of icy planetesimals.

The physical properties relevant to the evolution are examined in §2 including 1) the thermal conductivity, 2) the density and 3) the tensile strength. The physical properties of the ice discussed here include the activation energy of evolving processes of volatile molecules, and the effective latent heat of crystallization of amorphous H_2O ice. The ice composition in the planetesimal is assumed to be amorphous H_2O ice containing CO and CO_2 as impurities. The basic equations and results of the numerical calculations are presented in §3. It is revealed that evolution forks into three ways depending on the initial chemical composition of the ice in the planetesimals. They are:

1) Endothermic case, where both CO and CO_2 are contained in the ice in significant amount ($\sim 10\,\%$): The crystallization degree of amorphous H_2O ice is $40\,\%$, and CO trapped in the fraction of the ice is evolved at the final stage; this CO escapes outside of the planetesimal. On the other hand, CO_2 condenses on the surfaces of the dust grains immediately after crystallization of amorphous H_2O ice and is preserved. As the crystallization proceeds, sintering of CO_2 and H_2O takes place, and as a result the tensile strength is enhanced by three orders of magnitude.

2) Exothermic case, where the contents of both CO and CO_2 are smaller ($\sim 1\,\%$) than that of 1): Complete crystallization of the amorphous H_2O ice takes place and runaway temperature increase occurs up to about 140 K with increasing pressure gradient of CO and CO_2 vapors released from the ice. Sintering of CO_2 and H_2O leads to the tensile strength increased by three orders of magnitude as in the case of 1).

3) No CO_2 case, where CO is contained with considerable amount ($\sim 1\,\%$), but the CO_2 content is small ($\sim 0\,\%$). The evolution in this case is essentially the same as in the case 2) but disruption of the planetesimal occurs depending on the magnitude of the activation energy of surface diffusion of H_2O. If the activation energy is large, sintering of H_2O proceeds slowly. Consequently the pressure gradient due to CO vapors exceeds the tensile strength at some point, leading to disruption of the planetesimals.

Discussion is given in §4 on the implications of the results obtained in the previous sections. It is suggested that emergence of the diversity of planetary systems originates from the diversity of the composition of the ices in molecular clouds from which the planetary systems are formed. Namely, difference in the interstellar ice composition leads to different evolution described above. Discussion is given on the influences of the evolution of the tensile strength on collisional accretion to the cores of the Jovian planets. Conditions of the growth of the icy planetesimal are presented, and it is shown that the increase in the tensile strength in the icy planetesimals is necessary for forming the cores of the Jovian planets.

Contents

1 Introduction **4**

2 Physical quantities **7**
2.1 Thermal conductivity . . . 7
2.1.1 Thermal conductivity of a mixture of ices . . . 7
2.1.2 Comparison of the expressions of the effective thermal conductivities 12
2.1.3 Thermal conductivity of a dust grain . . . 12
2.1.4 Thermal conductivity of icy planetesimals . . . 13
2.2 Density of planetesimals . . . 13
2.3 Tensile strength . . . 16
2.3.1 Contact area between H_2O mantles . . . 17
2.3.2 Sintering of the icy mantles . . . 18
2.3.3 Surface diffusion coefficient . . . 19
2.3.4 Contact area increased by sintering . . . 21
2.3.5 Increased strength due to sintering . . . 22
2.4 Physical properties of ices . . . 22
2.4.1 Activation energies of evolving processes . . . 22
2.4.2 Latent heat of crystallization . . . 24

3 Evolution of icy planetesimals **28**
3.1 Basic equations . . . 28
3.1.1 Heat conduction equation . . . 28
3.1.2 Diffusion equation of volatile molecules . . . 30
3.1.3 Tensile stress distribution . . . 31
3.2 Numerical results . . . 32
3.2.1 Parameter values . . . 32
3.2.2 Endothermic model . . . 33
3.2.3 Exothermic model . . . 41
3.2.4 No CO_2 model . . . 47
3.3 Summary of the evolution . . . 51

4 Discussion **56**
4.1 Ices in molecular clouds . . . 56
4.2 Effects of the evolution of the tensile strength on formation of the Jovian planets . . . 57

5 Summary **58**

1 Introduction

This thesis is devoted to studies of materials evolution of icy planetesimals. Icy planetesimals are key objects in planetary formation processes. The cores of the Jovian planets are formed through mutual coagulation of the icy planetesimals (Hayashi et al. 1985). Kuiper belt objects are also products of mutual collisions of the icy planetesimals (Yamamoto et al. 1994). It is widely believed that cometary nuclei are the remnants of icy planetesimals (Yamamoto and Kozasa 1988). The grounds of this conjecture is that the nucleus contains rich volatile materials such as H_2O and CO ices, indicating the pristinity of the nucleus. Consequently, the icy planetesimals are key objects connecting the protoplanetary nebula and our present solar system. Although the presence of the Jupiter-sized planets are confirmed observationally around main-sequence stars (Mayor and Queloz 1995), it has been difficult to detect the swarm of planetesimals around young stars by the current observational state of the art. The icy planetesimal has remained a theoretical concept in the study of formation of the planets, and their evolution has been a missing-link between the interstellar molecular clouds and planetary systems.

An essential aspect presented in this thesis is the *materials* evolution of icy planetesimals. Although many studies on the *dynamical* evolution of the swarm of the planetesimals have been carried out (e.g. Ohtsuki et al. 1993) and have revealed the formation time scale of planets and the occurrence of the runaway growth of a protoplanet (Wetherill and Stewart 1989), the evolution of materials composing the planetesimals has been paid less attention. In most of studies on the *dynamical* evolution of the swarm of planetesimals, it is assumed that the planetesimals stick perfectly on a collision between them. However, the sticking probability of the planetesimals depends on the tensile strength of the planetesimals (Watanabe and Miyama 1992). Thus evolution of the tensile strength of the planetesimals is relevant to the dynamical evolution.

If Kuiper belt objects and cometary nuclei are indeed the remnants of icy planetesimals, their chemical compositions are the results of chemical evolution of the planetesimals. The compositions of volatile components of cometary nuclei have been investigated especially in detail for Comet Halley (Mumma et al. 1993) and recently for Comet Hale-Bopp by ISO satellite (Crovisier et al. 1997). Likewise, the surface composition of Kuiper belt object 1993SC has been estimated by IR absorption (Brown et al. 1997) and broad-band reflectance spectra (Luu and Jewitt 1996, Jewitt and Luu 1997). On the basis of these observed compositions of icy bodies, the investigation of the chemical evolution of the icy planetesimals makes the discussion possible on the chemical composition of the starting materials of our solar system. Moreover, we can discuss the chemical evolution of the planetesimals at the other planetary system, which will be formed from the interstellar ices currently observed around embedded sources in molecular clouds.

Accordingly, the evolution of the chemical composition and the tensile strength of the icy planetesimals are the main concern in this thesis in contrast to many studies on the evolution of short-period comets that concentrate mainly on the temperature evolution and the gas emission rate from the surface (e.g. Espinasse et al. 1991) in connection with cometary activity. The aim of this thesis is to clarify the materials evolution of the icy planetesimals and to reveal the missing-link between dust grains in molecular clouds and current objects in our solar system.

It is worth reviewing a brief history of the solar system formation from the molecular cloud stage to the stage of formation of the planets. In molecular clouds, dust grains consist of a silicate core, an icy mantle and organics (Greenberg 1982) and their size is typically $0.1\,\mu$m. The dust account for 1% of total mass of a molecular cloud. In recent years, the detailed chemical composition of the icy mantles in various molecular clouds comes to be measured especially by the ISO satellite (Kessler et al. 1996). The main component is amorphous H_2O ice, not crystalline ice, as revealed by the IR absorption spectra (Whittet et al. 1996). The ice contains volatile molecules such as CO and CO_2 as minor components. The composition differs from a cloud to a cloud, and the abundance of the minor components relative to H_2O ice varies from $< 1\,\%$ to the order of $10\,\%$ of H_2O (Whittet et al. 1996). The difference in the composition of the ice comes from the difference of the temperature, pressure, composition and oxidation state of the gas in the molecular cloud (Tielens et al. 1991). It has been pointed out that there are two kinds of ices (Tielens et al. 1991, Chiar et al. 1995): 1) polar ices whose dominant component is a polar molecule such as H_2O and CH_3OH and containing non-polar (or less-polar) molecule such as CO, CO_2, CH_4, etc as impurities, and 2) non-polar (or less-polar) ices whose dominant component is CO and CO_2.

The protoplanetary nebula (solar nebula) forms following gravitational collapse of a molecular cloud core (Shu et al. 1993), which leads to a central star surrounded by a disk-shaped nebula. The nebula consists of the gas and dust with the dust mass being $1\,\%$ in mass. The icy mantles on the grain surfaces were preserved outside 2.7 AU from the central star assuming the temperature distribution given by the Hayashi model (Hayashi et al. 1985). H_2O ice in the icy mantle contains volatile molecules such as CO, CO_2, CH_4, CH_3OH as confirmed their existence in molecular clouds. We take into account the two dominant species CO and CO_2, since the abundance of CH_4 ice is small ($\simeq 2\,\%$) and CH_4 molecules behave the same as CO in terms of volatility (§4.1), and CH_3OH is not contained in H_2O ice as impurity, but forms CH_3OH dominant ice (Chiar et al. 1996) and does not affect the thermal evolution of the icy planetesimals.

In the past years, it has been considered that the planetesimal is formed through the gravitational instability of the dust-rich layer in the solar nebula (Sekiya 1983). The diameter of the planetesimals thus formed is $\sim 10^6\,$cm at 1 AU. Weidenschilling and his co-workers (Weidenschilling and Cuzzi 1993, Weidenschilling 1997) have pointed out, however, that the instability is prevented by turbulence of the nebular gas induced by the velocity difference between the dust-rich layer near the midplane and the gas-rich layer above the dust-rich layer. In consequence the planetesimals must be formed by mutual coagulation of dust grains in the solar nebula instead of the gravitational instability. The coagulation processes have been investigated experimentally (Blum et al. 1993) and theoretically (Dominik and Tielens 1997, Sirono 1998). In any case, the resultant planetesimals are highly porous objects and their density is estimated to be $\simeq 0.5\,\mathrm{g\,cm^{-3}}$ (cf. §2.2), since the self-gravity of such a tiny object is too small to cause compaction of the dust aggregate. Therefore, the porous and particulate nature of the composing material of the icy planetesimals must be properly taken into account in the study of the evolution of the planetesimals.

The planetesimals evolve by their own internal energy sources such as radiogenic heating due to decay of ^{40}K, ^{235}U, ^{238}U and ^{232}Th contained in the silicate grains, and crys-

tallization of amorphous H_2O ice in the grain mantle. The radiogenic heating causes the temperature rise of the icy planetesimal and triggers further evolution caused by crystallization of amorphous H_2O ice. The crystallization results in the following consequences: 1) temperature increase (in some cases, *decrease* as seen later) due to release of the latent heat of crystallization, 2) the change in the chemical composition of the ice due to release of the volatile molecules trapped in the ice, 3) the increase in gas pressure in the pores by release of the volatile molecules, and 4) the increase in the tensile strength of the planetesimal caused by sintering of the volatile molecules at the neck between dust grains. Crystallization of the amorphous ice is thus the main cause of the materials evolution of the icy planetesimals.

There are three essential physical quantities that governs the evolution of the planetesimals: 1) their thermal conductivity, 2) the latent heat of crystallization of the amorphous H_2O ice containing the volatile molecules, and 3) the tensile strength of the planetesimals. One of the purposes of this thesis is to give proper expressions of these physical quantities of the icy planetesimals, and to apply the results to the evolution of the icy planetesimals.

This thesis is organized as follows: the physical quantities stated above are discussed in detail in §2. An expression of the thermal conductivity of the planetesimals is deduced by the effective medium theory. The density of the planetesimals is determined with the use of the constraint counting method. Cohesion mechanisms between dust grains are discussed and an expression of the tensile strength is given on the basis of the theory of elasticity and sintering. The evolving processes of the volatile molecules from the amorphous H_2O ice are examined and discussion is given on the latent heat of the amorphous H_2O ice containing CO and CO_2. §3 presents the basic equations describing evolution of the icy planetesimals and the results of the numerical calculations. It will be revealed that the evolution of the icy planetesimal forks into three ways depending on the chemical composition of the icy mantle. The implications of the results are discussed in §4. The interrelation among the ices in molecular clouds, in the icy planetesimals, and in the cometary nuclei is discussed. The effect of the evolution of the tensile strength of the icy planetesimals on accretion onto the Jovian planets is examined. The summary is given in §5.

Related publications are cited in appendices.

A) Sirono, S. and Yamamoto, T. 1997. Thermal conductivity of granular materials relevant to the thermal evolution of cometary nucleus. *Planetary and Space Science*, **45**, 827-834.

B) Sirono, S. and Yamamoto, T. 1998. Release mechanisms of volatile molecules in amorphous H_2O ice. to appear in *Formation and Evolution of Solids in Space*, (J. M. Greenberg, ed) Kluwer. in press.

2 Physical quantities

In this section, the physical quantities relevant to evolution of icy planetesimals are discussed in detail. The quantities are: 1) the thermal conductivity, 2) the density, 3) the tensile strength and 4) physical properties of ices including the activation energy of evolving processes of volatile molecules trapped in the ice and the effective latent heat of crystallization of amorphous H_2O ice.

2.1 Thermal conductivity

Evaluation of the thermal conductivity of icy planetesimals is very difficult because it involves shapes, positions, and contact areas of individual dust grains. In the study of the thermal evolution of cometary nucleus so far done, the effect of porosity of icy planetesimals, which is regarded as a dust aggregate, is modeled by putting cubic voids in a continuum medium (Espinasse et al. 1991), or by introducing a free parameter taking account of the nucleus porosity and configuration of dust grains (Haruyama et al. 1993). A similar difficulty is met in determining the thermal conductivity of a mixture of amorphous and crystalline H_2O ices, which appears in the course of the evolution in general. The non-realistic configuration of amorphous and crystalline ices has been assumed in most of the cometary studies (e.g. Espinasse et al. 1991), in which amorphous and crystalline ices are placed in parallel along the heat flow.

In this section we shall formulate the effective thermal conductivity of amorphous and crystalline ice mixtures and that of dust aggregates on the basis of the effective-medium theory (Kirkpatrick 1973), which was originally developed for a random-resistor network. The random-resistor network is a discrete system, whereas the mixture of amorphous and crystalline ice with which we are concerned is a continuum system. It will be shown that the formulas for discrete and continuum system are identical. The newly derived thermal conductivities are applied to examining thermal evolution of the icy planetesimal.

2.1.1 Thermal conductivity of a mixture of ices

Figure 1 shows a model of an icy planetesimal. The planetesimal is of porous structure composed of sub-micron-sized dust grains, each of which consists of a silicate core, an organic mantle, and an outer icy mantle (Greenberg 1982). H_2O ice in the mantle is initially amorphous since we are concerned with planetesimals formed sufficiently far from the Sun. In general, the ice becomes a mixture of amorphous and crystalline ices in the course of the thermal evolution. It is assumed that each dust grain is a sphere with the same radius. For simplicity we ignore the effect of the organic mantle on heat conduction in the aggregate, and of the presence of the volatile molecules other than H_2O in the ice. The thermal conductivity of an icy planetesimal is calculated via the following three steps:

1) Calculate the effective thermal conductivity κ_{H_2O} of the icy mantle, which is a mixture of amorphous and crystalline ices.

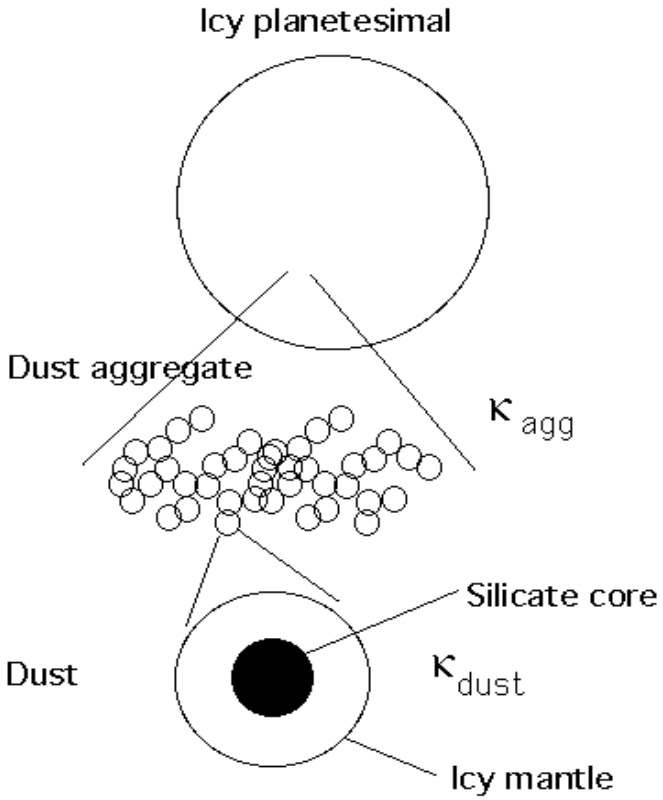

Figure 1: Schematic view of the structure of an icy planetesimal. The panels from upwards to downwards correspond to macroscopic to microscopic views.

2) Determine the thermal conductivity $\kappa_{\rm dust}$ of an individual grain, which is composed of the silicate core and the icy mantle with the use of the result of 1).

3) Calculate the effective thermal conductivity $\kappa_{\rm agg}$ of a whole planetesimal, which is a porous dust aggregate.

First, let us determine $\kappa_{\rm H_2O}$ (step 1). Consider a sphere of radius s and thermal conductivity κ centered at $\boldsymbol{r} = 0$ in a uniform medium of thermal conductivity $\kappa_{\rm H_2O}$. Under a uniform temperature gradient in the z-direction, $-(\partial T/\partial z)_0 (> 0)$, the steady-state temperature distribution is given by the solution of the Laplace equation

$$\Delta T = 0 \tag{1}$$

with the boundary conditions at $r = s$ that

$$T_1 = T_2, \tag{2}$$

and

$$\kappa \frac{\partial T_1}{\partial r} = \kappa_{\rm H_2O} \frac{\partial T_2}{\partial r}, \tag{3}$$

where suffices 1 and 2 denote the sphere and the effective medium, respectively. The solution to Eq. (1) in the sphere is given by

$$T_1(r, \theta) = -\frac{3\kappa_{\rm H_2O}}{\kappa + 2\kappa_{\rm H_2O}} \left(\frac{\partial T}{\partial z} \right)_0 r \cos\theta. \tag{4}$$

The heat flux in the z-direction in the sphere is thus given by

$$j_z(\kappa) = -\kappa \frac{\partial T_1}{\partial z} = -\frac{3\kappa_{\rm H_2O}\kappa}{\kappa + 2\kappa_{\rm H_2O}} \left(\frac{\partial T}{\partial z} \right)_0. \tag{5}$$

The thermal conductivity κ of the sphere equals either $\kappa_{\rm H_2O,c}$ or $\kappa_{\rm H_2O,a}$ depending on whether the sphere is crystalline or amorphous, respectively. When the volume fraction of crystalline ice is ξ, which we call crystallization degree hereafter, the probability distribution $P(\kappa)$ of the thermal conductivity κ is given by

$$P(\kappa) = \xi \delta(\kappa - \kappa_{\rm H_2O,c}) + (1 - \xi)\delta(\kappa - \kappa_{\rm H_2O,a}). \tag{6}$$

The effective thermal conductivity $\kappa_{\rm H_2O}$ of the medium with the crystalline degree ξ is determined self-consistently such that $j_z(\kappa)$ averaged over κ with the probability distribution $P(\kappa)$ equals $j_z(\kappa_{\rm H_2O})$:

$$\int_0^\infty d\kappa P(\kappa) j_z(\kappa) = j_z(\kappa_{\rm H_2O}), \tag{7}$$

which leads to

$$\frac{\kappa_{\rm H_2O} - \kappa_{\rm H_2O,c}}{\kappa_{\rm H_2O,c} + (1/\xi_{\rm c} - 1)\kappa_{\rm H_2O}} \xi + \frac{\kappa_{\rm H_2O} - \kappa_{\rm H_2O,a}}{\kappa_{\rm H_2O,a} + (1/\xi_{\rm c} - 1)\kappa_{\rm H_2O}} (1 - \xi) = 0, \tag{8}$$

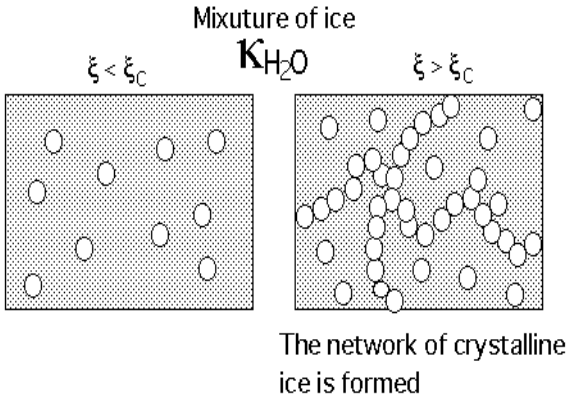

Figure 2: Percolation of crystalline ice in amorphous ice. When $\xi < \xi_{\rm c}$, the crystalline phases are isolated from each other. The crystalline ice comes to be connected throughout the medium when ξ becomes larger than $\xi_{\rm c}$, resulting in the increase in the effective thermal conductivity $\kappa_{\rm H_2O}$.

where $\xi_{\rm c}$ is called the percolation threshold (Stauffer and Aharony, 1994. see Fig. 2). Equation (8) determines the thermal conductivity of a *continuum* composite medium. It should be pointed out that Eq. (8) is identical to the expression of the electric conductivity of a *discrete* system described by a random-resistor network (see Eq. (5.6) of Kirkpatrick 1973). The same equation has been obtained by Landauer (1952) for the electrical resistance by a different derivation. The critical crystallization degree $\xi_{\rm c} = 1/3$ corresponds to the percolation threshold for a cubic lattice under the effective medium approximation (Kirkpatrick, 1973).

Figure 3 shows $\kappa_{\rm H_2O}(\xi)$ given by Eq. (8) as a function of the crystallization degree ξ. Here we take the thermal conductivity $\kappa_{\rm H_2O,a}$ of amorphous ice obtained by Kouchi et al. (1992) and that of crystalline ice $\kappa_{\rm H_2O,c}$ expressed (Haruyama et al 1993) by

$$\kappa_{\rm H_2O,a} = \kappa_{\rm a0} T = 7.1 \times 10^{-3} T \ {\rm erg\ cm^{-1}\ s^{-1} K^{-1}}, \tag{9}$$

$$\kappa_{\rm H_2O,c} = \kappa_{\rm c0}/T = 5.67 \times 10^{7}/T \ {\rm erg\ cm^{-1}\ s^{-1} K^{-1}} \tag{10}$$

at the relevant temperatures. We take $T = 100\,{\rm K}$ in Fig. 3 The thermal conductivity of the ice mantle is $\kappa_{\rm H_2O} \sim \kappa_{\rm H_2O,a}$ for $\xi < \xi_{\rm c}$ because $\kappa_{\rm H_2O,a} \ll \kappa_{\rm H_2O,c}$ in the relevant temperatures, implying that heat conduction is negligible practically. For $\xi > \xi_{\rm c}$, $\kappa_{\rm H_2O}$ can be approximated by

$$\kappa_{\rm H_2O} \simeq \kappa_{\rm H_2O,c} \frac{\xi - \xi_{\rm c}}{1 - \xi_{\rm c}} \tag{11}$$

from Eq. (8).

As is seen in Fig. 3, $\kappa_{\rm H_2O}(\xi)$ rises abruptly at $\xi_{\rm c} = 1/3$. This is because the crystalline phases isolated from each other at $\xi < \xi_{\rm c}$ come to be connected throughout the medium when ξ becomes larger than $\xi_{\rm c}$, resulting in the increase in the effective thermal conductivity $\kappa_{\rm H_2O}$ (see Fig. 2). The formation of this network plays an important role as will be seen later.

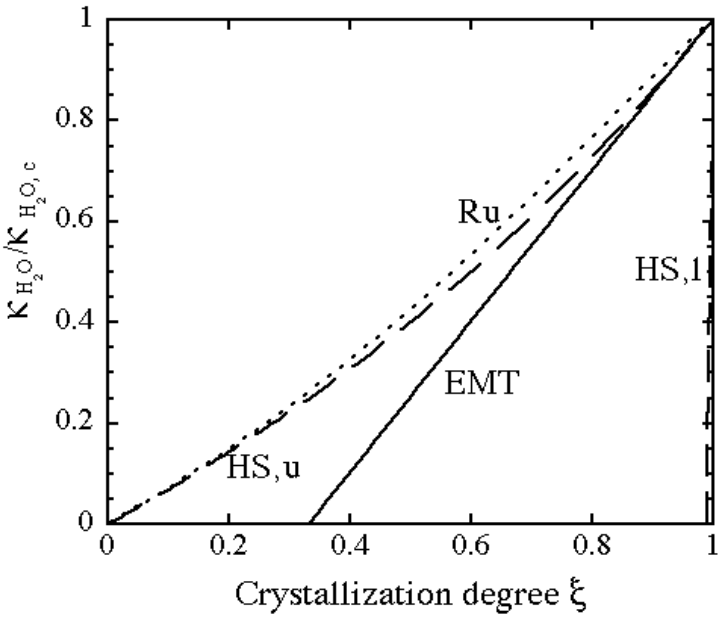

Figure 3: Thermal conductivities of a mixture of amorphous and crystalline ices versus the crystallization degree ξ. The line denoted by EMT is the result of this study (Eq. (8)). The percolation threshold is $\xi_c = 1/3$ at which the thermal conductivity increases abruptly. The dashed lines denoted by HS,u and HS,l are the upper and lower limits of the thermal conductivity of two component mixtures derived by Hashin and Shtrikman (1962). The dotted line denoted by Ru shows the effective thermal conductivity derived by Russel (1935). Note that the line EMT is between the upper and lower limit at all ξ in contrast to the dotted line Ru, which is above the upper limit at all ξ.

2.1.2 Comparison of the expressions of the effective thermal conductivities

It is worth comparing $\kappa_{\rm H_2O}$ given by Eq. (8) with other formulas of the effective thermal conductivities of two-component mixtures so far obtained. With the use of the variational principle, Hashin and Shtrikman (1962) derived the upper and lower bounds of the effective magnetic permeability of a composite medium in which each component is randomly distributed. In terms of the thermal conductivity, the lower bound $\kappa_{\rm HS,l}$ and the upper bound $\kappa_{\rm HS,u}$ are expressed by

$$\kappa_{\rm HS,l} = \frac{(1+2\xi)\kappa_{\rm H_2O,c} + 2(1-\xi)\kappa_{\rm H_2O,a}}{(1-\xi)\kappa_{\rm H_2O,c} + (2+\xi)\kappa_{\rm H_2O,a}}\kappa_{\rm H_2O,a}, \tag{12}$$

$$\kappa_{\rm HS,u} = \frac{2\xi\kappa_{\rm H_2O,c} + (3-2\xi)\kappa_{\rm H_2O,a}}{(3-\xi)\kappa_{\rm H_2O,c} + \xi\kappa_{\rm H_2O,a}}\kappa_{\rm H_2O,c}. \tag{13}$$

Russel's formula (Russel 1935) gives the effective thermal conductivity of a porous material. For a medium composed of amorphous and crystalline ices, Russel's thermal conductivity is written (see Capria et al. 1996) as

$$\kappa_{\rm R} = \frac{\left[1-(1-\xi)^{2/3}\right]\kappa_{\rm H_2O,c} + (1-\xi)^{2/3}\kappa_{\rm H_2O,a}}{\left[2-\xi-(1-\xi)^{2/3}\right]\kappa_{\rm H_2O,c} + \left[\xi+(1-\xi)^{2/3}-1\right]\kappa_{\rm H_2O,a}}\kappa_{\rm H_2O,c}, \tag{14}$$

in which it is assumed that cubes of one component are placed periodically in the medium of the other component.

It can be easily shown that 1) $\kappa_{\rm H_2O}$ given by Eq. (8) is within the upper and lower bounds given by Eq. (12) and (13), and 2) $d\kappa_{\rm HS,l}/d\xi = d\kappa_{\rm H_2O}/d\xi$ holds at $\xi = 0$, and $d\kappa_{\rm HS,u}/d\xi = d\kappa_{\rm H_2O}/d\xi$ at $\xi = 1$ (see Fig. 3). These results suggest that the effective thermal conductivity $\kappa_{\rm H_2O}$ given by Eq. (8) is a good approximation to the actual ones. It should be pointed out that the Maxwell formula (Maxwell 1904) is identical to the upper bound. On the other hand, it is shown that $\kappa_{\rm R}$ is always larger than $\kappa_{\rm HS,u}$ except at $\xi = 0$ and $\xi = 1$ in Fig. 3; this comes from the prescribed geometry adopted in deriving the Russel's formula.

2.1.3 Thermal conductivity of a dust grain

The thermal conductivity $\kappa_{\rm dust}$ of a dust grain with the mass fraction x of the silicate core, (step 2) is given by Haruyama et al. (1993) as

$$\kappa_{\rm dust} = \kappa_{\rm H_2O}\left[1 + \frac{3f^3(\kappa_{\rm core} - \kappa_{\rm H_2O})}{2\kappa_{\rm H_2O} + \kappa_{\rm core} - f^3(\kappa_{\rm core} - \kappa_{\rm H_2O})}\right], \tag{15}$$

where

$$f = \left[\frac{x\rho_{\rm H_2O}}{x\rho_{\rm H_2O} + (1-x)\rho_{\rm core}}\right]^{1/3} \tag{16}$$

is the ratio of the core radius to the dust radius. Equation (15) can be derived in the same way with the use of Eq. (5). It should be pointed out that $\kappa_{\rm dust}$ is of the same form as that of Haruyama et al. (1993) but the thermal conductivity of the icy mantle $\kappa_{\rm H_2O}$ is different

from theirs as given here by Eq. (11). We take the ice density $\rho_{H_2O} = 0.9\,\mathrm{g\ cm^{-3}}$ for both amorphous and crystalline ices, and the core density is taken to be $\rho_{\rm core} = 3.0\,\mathrm{g\ cm^{-3}}$. The thermal conductivity of the silicate core is taken to be $\kappa_{\rm core} = 10^5\,\mathrm{erg\ cm^{-1}s^{-1}K^{-1}}$, which is for fused quartz (Horai and Susaki, 1989).

2.1.4 Thermal conductivity of icy planetesimals

Finally, we derive the effective thermal conductivity $\kappa_{\rm agg}$ of the whole icy planetesimal (step 3). Equation (8) is also applicable to obtain the the thermal conductivity of a porous planetesimal because the equation for the discrete system (dust aggregate) is the same as the continuum system (mixture of ices) as we have shown. We model an icy planetesimal to be composed of elastic spherical grains of radius a placed randomly on the sites of a cubic lattice with a lattice constant of $2a$. Let each site be occupied by the grain with probability p and unoccupied with probability $1-p$. The thermal conductivity at an occupied site is $\kappa_{\rm dust}$, and that at an unoccupied site (pore) is zero. Replacing κ_{H_2O} by $\kappa_{\rm agg}$, $\kappa_{\rm H_2O,c}$ by $\kappa_{\rm dust}$, $\kappa_{\rm H_2O,a}$ by zero and ξ by p in Eq. (8), we obtain the thermal conductivity of the planetesimal as $\kappa_{\rm agg} = 3(p-p_{\rm c})\kappa_{\rm dust}/2$ with $p_{\rm c} = 1/3$ for a cubic lattice, if the limitation of the contact area between adjacent dust grains through which heat flows is ignored.

Actually, heat can flow only through the contact area S. We take this effect into account by multiplying

$$S^* \equiv S/ga^2, \tag{17}$$

where g is a geometrical factor that depends on the structure of the lattice. g is generally on the order of unity, and $g = 4$ for a cubic lattice. The thermal conductivity $\kappa_{\rm agg}$ of the planetesimal is thus written as

$$\kappa_{\rm agg} = \frac{3}{2}(p-p_{\rm c})S^*\kappa_{\rm dust}. \tag{18}$$

The contact area S will be determined in the next section.

It must be pointed out that p does not mean the volume fraction $\phi = 1 -$ porosity but means the fraction of packing. This is because one cannot fill space with spheres of identical sizes. For a cubic lattice, the relationship between p and ϕ is given by $\phi = [(4\pi/3)/2^3]p \simeq 0.52p$. We note that p should be larger than $p_{\rm c} = 1/3$ for the grains to be connected with each other to form the planetesimal although this is not sufficient condition for sustaining the self gravity of the planetesimal as seen in the next section.

2.2 Density of planetesimals

The thermal conductivity given by Eq. (18) and the permeability of the volatile molecules in the planetesimal depend on the density, or in other words, on the porosity of the planetesimal. The density of Comet Halley is estimated to be 0.28 to $0.65\,\mathrm{g\,cm^{-3}}$ (Rickman 1989). Recently, the density of asteroid 253 Mathilde has been estimated to be $1.3\,\mathrm{g\,cm^{-3}}$ by tracking the trajectory of NEAR spacecraft (Yeomans et al. 1997). There has been no theoretical estimate of the density of such porous objects. We shall estimate the density of planetesimals on the basis of geometrical argument.

Consider an aggregate consisting of $N_{\rm d}$ identical spherical dust grains. These grains contacts each other by the van der Walls attraction. There are four different types of relative motions of grains in contact such as rolling, sliding, stretching and twisting. Deformation of the aggregate under stress is initiated by rolling motion between grains, because the energy necessary for the rolling motion is the smallest among four types of relative motion as shown by Dominik and Tielens (1997; hereafter D&T). The highest density at which only rolling motion is allowed can be estimated by the constraint counting method (Jacobs and Thorpe 1996) as follows. The total degrees of freedom of motion of the aggregate is $6N_{\rm d}$ since there are $N_{\rm d}$ dust grains and each dust grain has six degrees of freedom. A contact of a pair of grains loses 4 degrees of freedom (each one for stretching and twisting and two for sliding). As a result the remaining degrees of freedom N_f of the aggregate can be written as

$$N_{\rm f} = 6N_{\rm d} - \frac{4}{2}N_{\rm d}z, \tag{19}$$

where z is the average number of coordination of the dust grain. Division by two comes from the fact that a contact involves two grains. It is expected that the aggregate cannot deform by rolling alone when $z = 3$ for which $N_{\rm f} = 0$. This estimate has been proved to be quite good by numerical calculations as well (Thorpe and Garboczi 1987, Jacobs and Thorpe 1996). After that, the deformation of an aggregate should involve the other types of motion than rolling such as sliding. This transition leads to the change in the compressive yield stress of the aggregate.

Let us estimate the compressive yield stress against rolling, when the volume fraction occupied by the grains is low enough. It is assumed that the grains of identical radius a are arranged to form a distorted cubic lattice whose typical length of a side is $l = 2ca$ (see Fig. 4), where c is a constant and is estimated to be $c \simeq \sqrt{2\pi/\phi}$ for $\phi \ll 1$. The relation between torque M against rolling at a contact area and the displacement $\eta\,(\ll a)$ of the center of the grain relative to its initial position is given by $M = 12\pi\gamma a\eta$ (D&T), where γ is the surface energy of the material. If we apply force F to both ends of a curved side of the lattice, elastic deformation occurs mostly at a contact area of maximum torque along the side. Then the torque is roughly given by $M = 12\pi\gamma a\eta = lF\sin\theta$, where θ is the angle between the normal vector of the contact area and the external force. With increasing the displacement η, rolling motion becomes irreversible. The critical η is on the order of the molecular (or atomic) radius of the grain material ($\eta_{\rm c} \sim 1 \times 10^{-8}\,{\rm cm}$). On the other hand, the stress P can be written macroscopically in terms of the force F as $P \sim F/l^2$. Substituting the expressions for F and l, the yield stress against rolling $P_{\rm cr}$ is thus given by

$$P_{\rm cr} = \frac{3\pi\gamma\eta_{\rm c}}{2c^3a^2\sin\theta}. \tag{20}$$

where we take $\sin\theta = 1/2$ and $c = 5$ as representative values.

When the volume fraction ϕ becomes large, resistance against sliding between grains sustains the external stress. With the use of the expression of the critical force $F_{\rm fric}$ for initiating sliding of the grain (D&T), the yield stress $P_{\rm cs}$ is roughly evaluated as

$$P_{\rm cs} = \frac{Ga_{\rm s}^2\phi}{16a^2}, \tag{21}$$

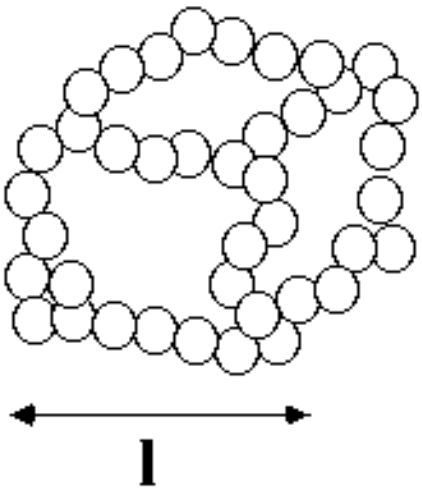

Figure 4: A schematic view of a lattice in the dust aggregate. Each lattice consists of a distorted line of dust grains connected each other.

where G is the shear modulus of the grain material, and $a_{\rm s}$ is the radius of the contact area between grains given by the JKR theory (Johnson 1985, Choksi et al. 1993) as

$$a_{\rm s} = \left(\frac{9\pi\gamma a^2 (1-\nu^2)}{E} \right)^{1/3}, \tag{22}$$

where E is Young's modulus and ν is Poisson's ratio.

Figure 5 illustrates $P_{\rm cr}$ and $P_{\rm cs}$ for H_2O ice. We adopt the following values of $E_{\rm H_2O} = 9.0 \times 10^{10}\,{\rm erg\,cm^{-3}}$, $\nu_{\rm H_2O} = 0.34$ (Gold 1958), $G_{\rm H_2O} = 2.8 \times 10^{10}\,{\rm erg\,cm^{-3}}$ and $\eta_{\rm c} = 1 \times 10^{-8}\,{\rm cm}$ (D&T). The surface energy $\gamma_{\rm H_2O}$ between H_2O ice is estimated from the van der Walls energy between a pair of H_2O molecules, since the dust grains are initially connected with each other not by the hydrogen bonding but by the van der Walls attraction force. The surface energy $\gamma_{\rm H_2O}$ due to van der Walls force is evaluated to be $\gamma_{\rm H_2O,v} = \varepsilon_{\rm H_2O}/4r_{\rm H_2O}^2 = 7.6\,{\rm erg\,cm^{-2}}$, where $\varepsilon_{\rm H_2O} = 7.6 \times 10^{-3}\,{\rm eV}$ is the van der Walls attraction energy of a pair of H_2O molecules (Greenberg, et al. 1995) and $r_{\rm H_2O} = 1.98 \times 10^{-8}\,{\rm cm}$ (see §2.2.2).

Figure 5 indicates that $P_{\rm cs}$ against sliding is much larger than $P_{\rm cr}$ for rolling. The compressive stress by self-gravity of a planetesimal of 10 km radius is on the order of $10^4\,{\rm dyn\,cm^{-2}}$. The planetesimal should be compacted up to $z = 3$ as discussed above, but further compaction does not take place since $P_{\rm cs} \gg 10^4\,{\rm dyn\,cm^{-2}}$ as seen in Fig. 5. For evaluation of the porosity of the aggregate, assuming that spherical dust grains of the same size are aggregated at cubic lattice sites, the fraction of packing p (see §2.1.4) is related to the average number of coordination as $z = z_{\rm max}p^2$ where $z_{\rm max}$ is the number of the adjacent sites. The factor p^2 comes from the fact that the probability of the appearance

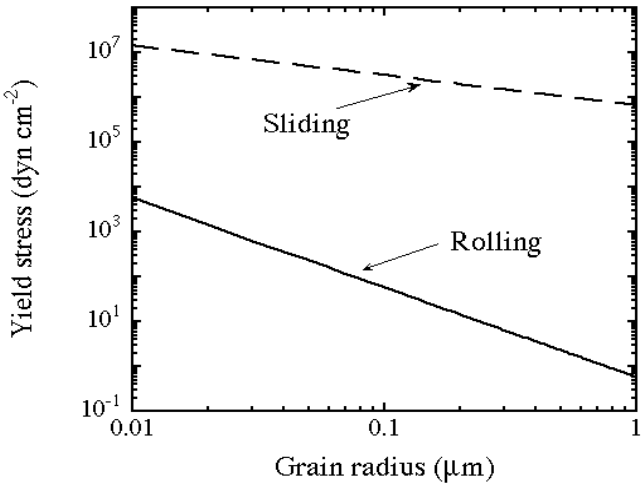

Figure 5: Yield stresses of a dust aggregate. The solid line stands for the yield stress $P_{\rm cr}$ due to rolling friction between dust grains, and the dashed line for sliding $P_{\rm cs}$.

of a connection between adjacent sites is p^2. For $z = 3$ and $z_{\rm max} = 6$ (for cubic lattice), we have $p = 0.71$ or the volume fraction $\phi = \phi_1 p = 0.37$ where $\phi_1 = 0.52$ is the maximum volume fraction when $p = 1$. The density of the planetesimal corresponding to $z = 3$ is given by

$$\rho = \frac{\phi}{\dfrac{x}{\rho_{\rm core}} + \dfrac{1-x}{\rho_{\rm H_2O}}}, \tag{23}$$

which gives $\rho = 0.51\,{\rm g\,cm^{-3}}$ for $x = 0.5$.

For comparison, let us calculate the density ρ for the closest packing ($z_{\rm max} = 12$). The average number of coordination z equals 3 as well since the arguments for deriving Eq. (19) is independent of the lattice. For the closest packing lattice, we have $\phi_1 = 0.72$, which give $\rho = 0.50\,{\rm g\,cm^{-3}}$ for $x = 0.5$ from Eq. (23).

2.3 Tensile strength

When CO is contained in the icy mantles of surfaces of grains in planetesimals, CO is evolved simultaneously with crystallization of amorphous H_2O ice. If the rate of release of CO contained in the icy mantle is sufficiently high, CO vapor accumulates in the pore. With increasing CO pressure, the pressure gradient of CO vapor overwhelms the tensile strength, leading to disruption of a planetesimal. The tensile strength is also relevant to the collisional evolution of the planetesimals. It has been found that a collision of two planetesimals of high tensile strength leads to formation of a massive planetesimal (Watanabe and Miyama 1992). The increase in the tensile strength accelerates formation

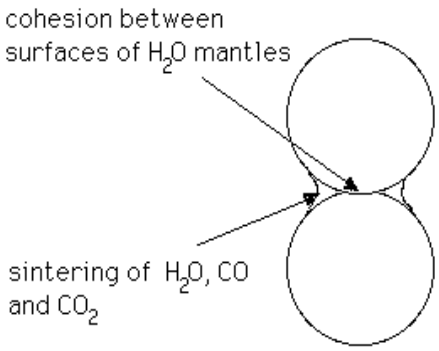

Figure 6: A schematic view of the structure of a neck between adjacent dust grains. The contact area consists of two parts. One is the area formed by the surface energy of H_2O mantle. The other is the additional area due to sintering of H_2O, CO and CO_2.

of the cores of the Jovian planets.

According to Greenberg et al. (1995), the tensile strength T of the icy planetesimal can be evaluated from the cohesive energy per unit volume of the icy planetesimal to be

$$T = \frac{3\phi z\gamma}{4\pi a^3} S, \tag{24}$$

where S is the contact area between a pair of grains, γ is the surface energy of the grain material, ϕ is the volume fraction of the dust grains in the planetesimal and z is the average coordination number of the dust grains, for which we put $z = 3$. Equation (24) is valid for the grain mantles composed of one species of volatile molecules such as H_2O. If the grain mantle of volatile molecules more than one species, the strength is a sum of contributions from different species (see §2.3.5).

The contact area S consists of two areas corresponding to different cohesion mechanisms between dust grains; one is contact area S_{H_2O} between the surfaces of H_2O icy mantles, and the other is enlarged area $S_{\rm sint}$ as a result of sintering of the grain mantles. A schematic picture is illustrated in Fig. 6. The tensile strength increases with increasing $S_{\rm sint}$.

2.3.1 Contact area between H_2O mantles

The contact area S_{H_2O} between the icy mantles of adjacent dust grains having surface energy $\gamma_{H_2O,v}$ adhering with each other is given by Eq. (22)

$$S_{H_2O} = \pi \left[\frac{9\pi\gamma_{H_2O,v} a^2 (1-\nu_{H_2O}^2)}{E_{H_2O}} \right]^{2/3}, \tag{25}$$

The contact area for the grains of radius $a = 0.1\,\mu$m is $S = 1.1 \times 10^{-12}\,$cm^2 and the normalized contact area is $S^* = 2.8 \times 10^{-3}$ for a cubic lattice for which $g = 4$ (see

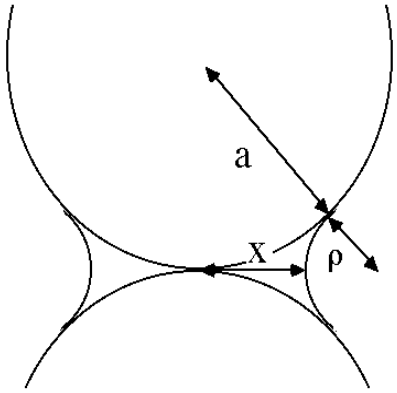

Figure 7: A schematic view of the contact area between the adjacent grains, where x and ρ stand for radii of curvature of the side surface of the neck and a for the grain radius.

Eq. (17)). For the physical quantities appeared in Eq. (25), we used the values given in §2.2. Substituting S_{H_2O} into Eq. (24), the tensile strength due to contact of the H_2O mantles is $T = 2.2 \times 10^3\,\mathrm{dyn\,cm^{-2}}$.

2.3.2 Sintering of the icy mantles

At the relevant temperatures in the evolution of the icy planetesimals, the most effective sintering mechanism is surface diffusion of H_2O, CO, and CO_2 molecules on the grain mantles among six processes of sintering (Swinkels and Ashby 1981, Maeno and Ebinuma 1983). The effect of the external stress on sintering is neglected for simplicity in this thesis.

Surface diffusion is driven by the gradient of the concentration of lattice vacancies (holes) on the surface of the icy mantle. The concentration gradient originates from the curvature of the side surface of the neck, where negative pressure is induced. When there is no curvature, the concentration n_h on the holes at the surface is given by

$$n_\mathrm{h} = n_\mathrm{s} \exp\left(-\frac{E_\mathrm{f}}{kT}\right), \tag{26}$$

where n_s is the number density of the molecule at the surface ($\mathrm{cm^{-2}}$), and E_f the formation energy of a hole. E_f at the neck with radii of curvatures ρ and x is effectively reduced by $\Omega\gamma(1/\rho - 1/x)$, where γ is the surface energy and Ω is the molecular volume of the species composing the icy mantle. It is assumed that the shape of the side surface of the neck is a part of a torus whose inner radius is ρ. It is easily shown that there is a relation that $\rho = x^2/2(a-x)$ (Swinkels and Ashby 1981). The concentration n_neck is then given by

$$n_\mathrm{neck} = n_\mathrm{s} \exp\left[-\frac{1}{kT}\left\{E_\mathrm{f} - \Omega\gamma\left(\frac{1}{\rho} - \frac{1}{x}\right)\right\}\right] \tag{27}$$

Then the increment of the concentration, Δn_h, of the hole at the side surface of the neck compared with the concentration n_h for the plane surface (see Fig. 6) can be evaluated

(Kuczynski 1949) to be

$$\begin{aligned}\Delta n_{\rm h} &= n_{\rm neck} - n_{\rm h} \\ &\simeq \frac{\gamma\Omega}{kT}\left(\frac{1}{\rho}-\frac{1}{x}\right) n_{\rm h}, \end{aligned} \tag{28}$$

where we have used the fact that $\Omega\gamma/\rho kT \ll 1$. The growth rate dV/dt of the volume of the neck is given as the product of the flux of the holes on the surface times the length through which the holes pass by

$$\frac{dV}{dt} = A\Omega D_{\rm h}\nabla n_{\rm h}, \tag{29}$$

where $D_{\rm h}$ is the diffusion coefficient of the holes on the surface, and $A = 4\pi x$ is the length of the circumference of the neck multiplied by two, which comes from the fact that the holes diffuse to both upper and lower grains in Fig. 7. The gradient $\nabla n_{\rm h}$ is roughly evaluated as $\nabla n_{\rm h} \simeq \Delta n_{\rm h}/\rho$. Then the growth rate dV/dt can be written as

$$\begin{aligned}\frac{dV}{dt} &= 4\pi x\Omega D_{\rm h}\frac{\gamma\Omega}{\rho kT}\left(\frac{1}{\rho}-\frac{1}{x}\right) n_{\rm h} \\ &= \frac{4\pi r x\gamma\Omega}{\rho kT} D_{\rm s}\left(\frac{1}{\rho}-\frac{1}{x}\right), \end{aligned} \tag{30}$$

where $D_{\rm s}$ is the surface self-diffusion coefficient of the molecules, and r is radius of the molecules. In Eq. (30), we have used the relation that $D_{\rm h}|\nabla n_{\rm h}| = D_{\rm s}|\nabla n_{\rm s}| \simeq rD_{\rm s}/\Omega\rho$. There are three equivalent sets of equations for H_2O, CO and CO_2. In sintered H_2O ice, H_2O molecules are bonded by hydrogen bonding in contrast with the case of grain adhesion by the van der Walls attraction (see §2.2). In this case we have $\gamma_{H_2O} = 100\ {\rm erg\,cm^{-2}}$ (Hobbs 1974). The surface energy of solid CO_2 is approximated by that of liquid CO_2 extrapolated to 0 K to be $\gamma_{CO_2} = 67.5\ {\rm erg\,cm^{-2}}$ (Pearce and Haniff 1987). Likewise, the surface energy of solid CO is approximated by that of liquid CO at 70 K to be $\gamma_{\rm CO} = 12.1\ {\rm erg\,cm^{-2}}$ (Handbook of Chemistry and Physics 1981). We take $\Omega_{H_2O} = 3.25 \times 10^{-23}\,{\rm cm^3}$ (Kouchi et al. 1994), $\Omega_{\rm CO} = 5.87 \times 10^{-23}\,{\rm cm^3}$ and $\Omega_{CO_2} = 4.57 \times 10^{-23}\,{\rm cm^3}$ (Handbook of Chemistry and Physics 1981). The radii of the molecules are deduced from these values as $r = (3\Omega/4\pi)^{1/3}$ leading to $r_{H_2O} = 1.98 \times 10^{-8}\,{\rm cm}$, $r_{\rm CO} = 2.41 \times 10^{-8}\,{\rm cm}$, and $r_{CO_2} = 2.22 \times 10^{-8}\,{\rm cm}$. We have neglected possible interactions among three kinds of molecules for simplicity.

The equations above to describe the rate of sintering are valid during the so-called stage 1 of sintering processes as defined by Swinkels and Ashby (1981). The stage 1 ends when x reaches $2a/3$ since the right-hand side of Eq. (28) becomes zero. The stage 1 is followed usually by formation of isolated pores (stage 2). If the stage 2 takes place actually in the planetesimal, the gas pressure increases monotonically in the pores, and it may causes the outburst of the planetesimal. The possibility of the occurrence of the stage 2 is questionable, however, in such a highly porous ($\phi \simeq 0.4$) dust aggregate.

2.3.3 Surface diffusion coefficient

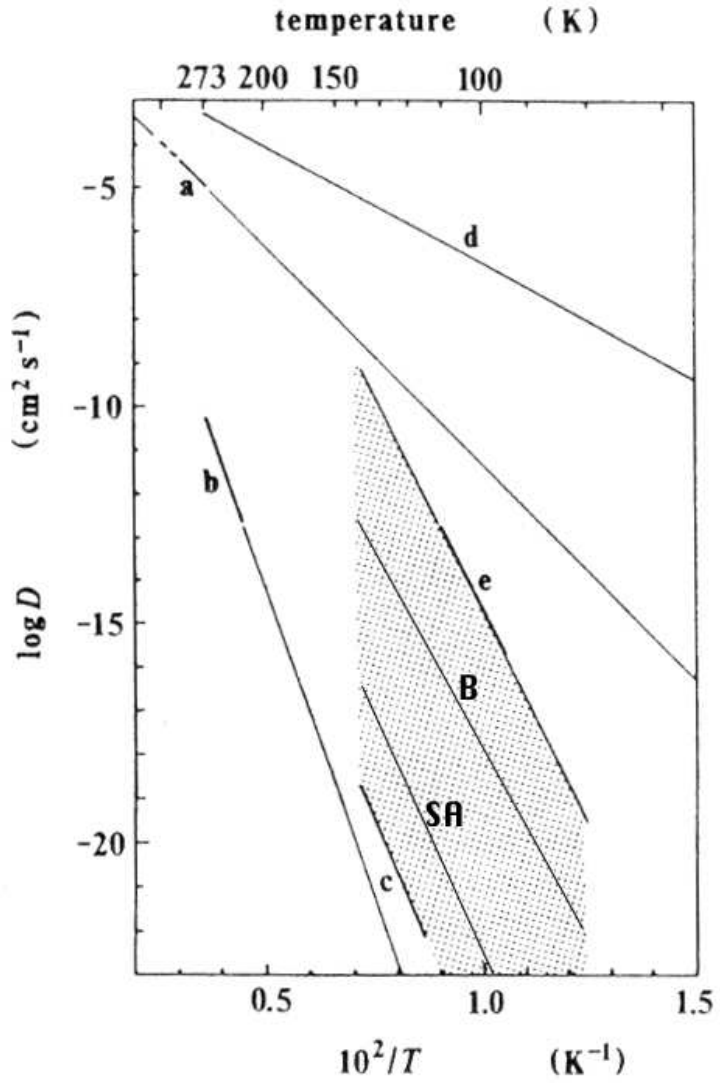

Figure 8: Self diffusion coefficients of H_2O in (a) liquid water, (b) ice I_h and (c) amorphous ice, and surface diffusion coefficients of H_2O on the surfaces of (d) the (0001) face of I_h and (e) polycrystalline ice I_c (from Kouchi et al. 1994). Kouchi et al. (1994) estimates the surface diffusion coefficient of H_2O on amorphous H_2O ice to be in the shaded part. The solid lines denoted by B and SA are the extrapolations from the experimental results obtained by Berland et al. (1995) and Sandford and Allamandola (1988), respectively. Note that both lines are in the shaded region estimated by Kouchi et al. (1994).

H_2O, CO and CO_2 molecules migrate to the neck by the processes discussed in the previous section. The essential physical quantity in sintering is the surface diffusion coefficient of each kinds of molecular species on amorphous H_2O ice. The surface diffusion coefficient D_s can be written as

$$D_s = D_{s0} e^{-E_s/T}, \tag{31}$$

where E_s is the activation energy of surface diffusion. Unfortunately, the activation energy E_s is difficult to measure experimentally and has large uncertainty. The activation energy of H_2O molecules is reported to be 3575K (Berland et al. 1995) indirectly from measurements of refractive index of amorphous H_2O ice. On the other hand, the surface binding energy of H_2O molecule on amorphous H_2O ice is measured as 4815K (Sandford and Allamandola 1988). Both experimental values may be used as the activation energy in the current status of the measurement. We denote both experimental values by $E_{s,SA}(H_2O)$ and $E_{s,B}(H_2O)$, respectively for convenience in the following sections. The coefficient $D_{s0}(H_2O)$ is estimated to be 0.02 for H_2O (Berland et al. 1995).

Figure 8 summarizes various diffusion coefficients of H_2O molecules on and in H_2O ice. Kouchi et al. (1994) estimates the surface diffusion coefficient of H_2O on amorphous H_2O ice to lie in the shaded region in Fig. 8. The solid lines denoted by B and SA indicate the surface diffusion coefficient by Berland et al. (1995) and Sandford and Allamandola (1988), respectively. As discussed later, the uncertainty in the activation energy E_{s,H_2O} greatly affects evolution of the icy planetesimals. Accordingly, all numerical calculations were performed for both activation energies of H_2O molecules by Berland et al. (1995) and Sandford and Allamandola (1988).

Since the activation energies of CO and CO_2 on amorphous H_2O ice surface is not available, as the activation energies here we take the binding energies of CO and CO_2 on amorphous H_2O ice measured to be 1780 K and 2860K, respectively (Sandford and Allamandola 1990). For $D_{s0}(CO)$ and $D_{s0}(CO_2)$, we use $D_{s0}(H_2O)$, since there are no experimental data for these molecules. This substitution does not much affect the results because the rates of sintering of CO and CO_2 are sufficiently high in any case because of the small activation energy of surface diffusion of these molecules.

2.3.4 Contact area increased by sintering

It is necessary to express the surface area S_{sint} formed by sintering in terms of the volume V of the neck. A simple calculation leads to $V(\rho)$ as a function of ρ as (see Fig. 7)

$$\begin{aligned} V(\rho) &= 2\pi\rho^2 a - \pi a \left(\frac{\rho a}{\rho + a}\right)^2 \\ &- \pi\sqrt{\rho^2 + 2\rho a}\left\{\rho^2 \sin^{-1}\left(\frac{a}{\rho + a}\right) + \frac{\rho^2 a}{(\rho + a)^2}\sqrt{\rho^2 + 2\rho a}\right\}. \end{aligned} \tag{32}$$

On the other hand, the area $S_{sint}(\rho)$ of the neck as a function of ρ is given by

$$\begin{aligned} S_{sint}(\rho) &= \pi x^2 \\ &= 2\pi\left\{\rho^2 + \rho a - \rho\sqrt{\rho^2 + 2\rho a}\right\}, \end{aligned} \tag{33}$$

where we have used $\rho = x^2/2(a-x)$ and neglected the area $S_{\rm H_2O}$ which exists irrespective of sintering, since $S_{\rm sint} \gg S_{\rm H_2O}$ is realized almost in the whole evolution. From Eqs. (32) and (33), $S_{\rm sint}$ may be expressed as a function of the volume V. The numerical calculations lead to the approximate relation given by

$$\frac{S_{\rm sint}}{\pi a^2} = \left(\frac{3V}{\pi a^3}\right)^{\alpha}, \tag{34}$$

where $\alpha = 0.48$. The contact area S between adjacent dust grains is written by

$$S = S_{\rm H_2O} + S_{\rm sint}(V). \tag{35}$$

This expression is used in Eq. (17) together with Eq. (34).

2.3.5 Increased strength due to sintering

The increased strength due to sintering to be added to the RHS of Eq. (24) is given by replacing $S_{\rm H_2O}$ by $S_{\rm sint}$ and $\gamma_{\rm H_2O}$ by $\gamma_{\rm sint}$ in Eq. (24). The surface energy of the neck $\gamma_{\rm sint}$ is left to be evaluated since the neck after sintering is a mixture of H_2O, CO and CO_2.

Consider a plane in the mixture of H_2O, CO and CO_2 ices. We denote the volume fraction of H_2O by $\phi_{\rm H_2O}$, CO by $\phi_{\rm CO}$, and CO_2 by $\phi_{\rm CO_2}$. If we assume that each kind of molecule is placed randomly, the fraction of the area on the plane occupied by H_2O is $\phi_{\rm H_2O}$, that of CO by $\phi_{\rm CO}$ and that of CO_2 by $\phi_{\rm CO_2}$. The surface energy of the neck $\gamma_{\rm sint}$ is thus evaluated to be

$$\gamma_{\rm sint} = \phi_{\rm H_2O}\gamma_{\rm H_2O,h} + \phi_{\rm CO}\gamma_{\rm CO} + \phi_{\rm CO_2}\gamma_{\rm CO_2}. \tag{36}$$

with

$$\phi_{\rm H_2O} + \phi_{\rm CO} + \phi_{\rm CO_2} = 1. \tag{37}$$

The surface energy of H_2O is not $\gamma_{\rm H_2O,v}$ but $\gamma_{\rm H_2O,h}$, since the cohesive mechanism in the neck is the hydrogen bonding (cf. §2.2.1). We take $\gamma_{\rm H_2O,h} = 100\ {\rm erg\,cm^{-2}}$ (Hobbs 1974). In consequence, the tensile strength with grains being sintered in the icy planetesimal is given by

$$T = \frac{3\phi z\gamma_{\rm H_2O,v}}{4\pi a^3} S_{\rm H_2O} + \frac{3\phi z\gamma_{\rm sint}}{4\pi a^3} S_{\rm sint}, \tag{38}$$

instead of Eq. (24).

2.4 Physical properties of ices

2.4.1 Activation energies of evolving processes

Figure 9 shows the result of sublimation experiment by Kouchi (1990). Amorphous H_2O ice containing 20% of CO is heated at the rate of $1\,{\rm K\,min^{-1}}$. It can be seen that CO is evolved at several temperatures. The chemical composition of the icy mantle in planetesimals changes with the evolving processes. The amorphous H_2O ice retains small amount of CO up to about 160 K (peak g in Fig. 9) at which H_2O itself sublimates, whereas pure CO sublimates at 23 K.

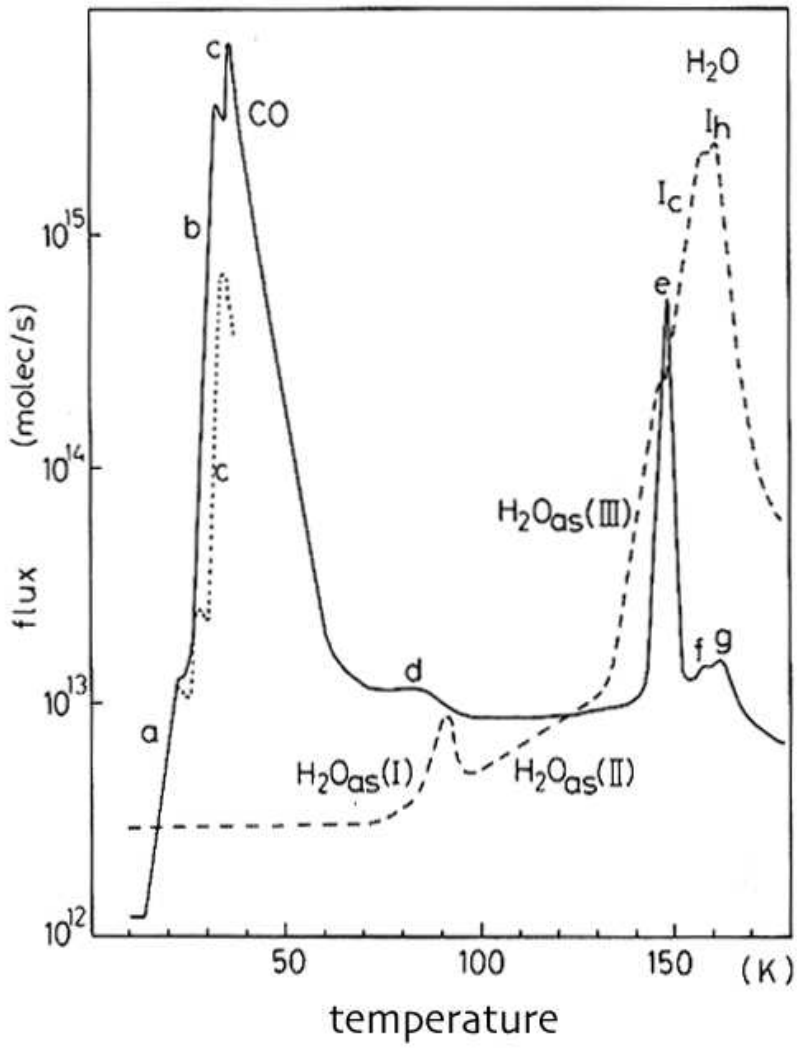

Figure 9: A plot of evolved CO (solid line) and H_2O (dashed line) flux. A desorption curve of CO from H_2O_{as} is added by the dotted line. The peaks a to g correspond to the different evolving mechanisms of CO (from Kouchi (1990)).

Kouchi (1990) attributed each peak of CO release to four processes: 1) sublimation of pure CO at 14 and 23 K (peaks a and b), 2) sublimation of CO adsorbed on the surface of amorphous H_2O ice at 34 K (peak c), 3) release of CO at several temperatures between 80 and 150 K (peaks d, e, and f), and 4) co-sublimation of H_2O and CO at 160K (peak g). The most important is peak e since the peak e is large and the temperature range overlaps the temperature attained in the icy planetesimal in the course of its evolution as seen later. The physical mechanism of the peak e is, however, uncertain. Kouchi (1990) and Bar-Nun et al. (1985) conjectured that the underling process of the peak e was squeezing-out of CO induced by crystallization of amorphous H_2O ice. On the other hand, Sandford and Allamandola (1988) attributed the peak e to diffusion of CO in amorphous H_2O ice.

For astrophysical interest, the activation energies of both processes proposed above (squeezing-out and diffusion) are crucial physical quantities that determine the evolving rate of the volatile molecules and the temperatures at which remarkable degassing is observed. Sirono and Yamamoto (1998) (appendix b) investigated both processes in detail, and found the relation between the activation energies and the temperatures of the peak.

In this thesis, only the peak e in Fig. 9 is taken into account in the evolution of icy planetesimals since the other two large peaks b and c are not relevant to the evolution (cf §4.1). Furthermore, it is assumed that the physical process leading to the peak e is squeezing-out induced by crystallization of amorphous H_2O ice (see Eq. (54)) as is suggested by the coincidence of the temperatures of the peak e and of crystallization of amorphous H_2O ice to crystalline ice I_h (see Fig. 9).

2.4.2 Latent heat of crystallization

Kouchi (personal communication, 1997) has found that crystallization of amorphous H_2O ice is an endothermic process when sufficient volatile molecules are contained in amorphous H_2O ice. Figure 11 shows the result of the differential thermal analysis (DTA) of crystallization of amorphous H_2O ice containing 10% of CO (Kouchi, personal communication). It is suggested (Kouchi, personal communication) that the endothermicity originates from taking-away of latent heat of sublimation of CO molecules evolving with crystallization of amorphous ice. As a result, the latent heat of crystallization becomes apparently negative. On the other hand, crystallization of pure amorphous H_2O ice is exothermic as seen in Fig. 10. Likewise, Fig. 12 shows the result of the DTA analysis of crystallization of the amorphous H_2O ice containing 10% of CO_2 (Kouchi, personal communication), which is also an endothermic process. Comparison Figs. 11 and 12 indicates that the sublimation heat of CO_2 is larger than that of CO because the peak in Fig. 12 is larger than that of Fig. 11.

Heat of sublimation of evolved CO and CO_2, denoted by H_{CO} and H_{CO_2}, respectively, is calculated by comparing the shaded areas of the peaks appeared in Figs. 10 to 12. The results are shown in Table 1. For comparison, the surface binding energies of H_2O-CO and H_2O-CO_2 measured by Sandford and Allamandola (1990) are also shown in Table 1. It can be seen that the our values are larger than the surface binding energy measured by Sandford and Allamandola (1990). This difference seems to come from the number of bonds of desorbing CO and CO_2 molecules with adjacent H_2O molecules to be cut at

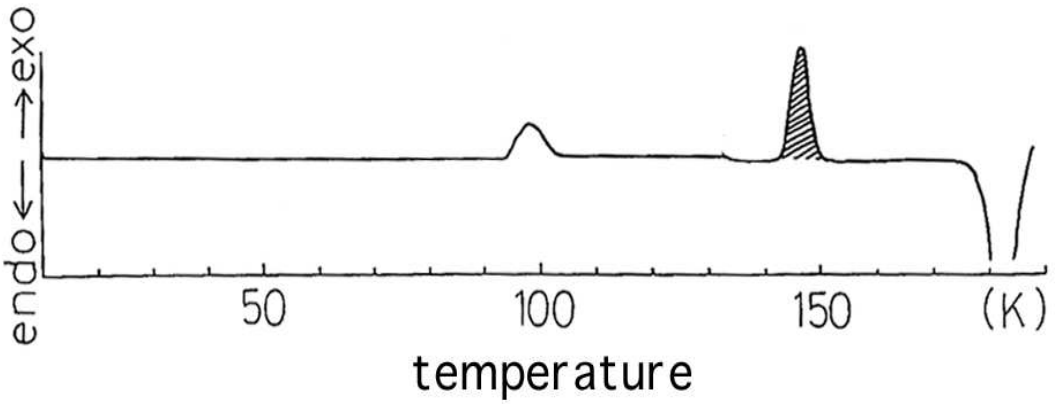

Figure 10: Differential thermal analysis scan of pure H_2O ice. The y axis is of an arbitrary scale. The peak at 145 K shows that crystallization of pure amorphous H_2O ice is an exothermic process. The peak at 100 K corresponds to the phase transition from a-H_2O(I) to (II) (Kouchi, personal communication).

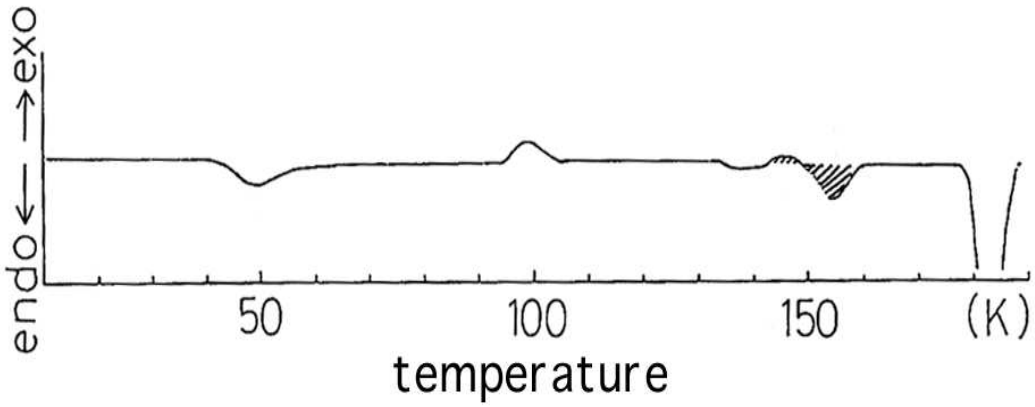

Figure 11: Same as in Fig. 10 but for H_2O ice containing 10% of CO. The y axis is of an arbitrary scale. Note that the peak at 145 K is reversed to that of Fig. 10 indicating that crystallization of H_2O ice containing 10% of CO is an endothermic process in contrast to Fig. 10. The negative peak at 50 K corresponds to desorption of CO. The sublimation energy of CO at crystallization of amorphous H_2O ice is calculated by comparing the shaded areas in Figs. 10 and 11 (Kouchi, personal communication)

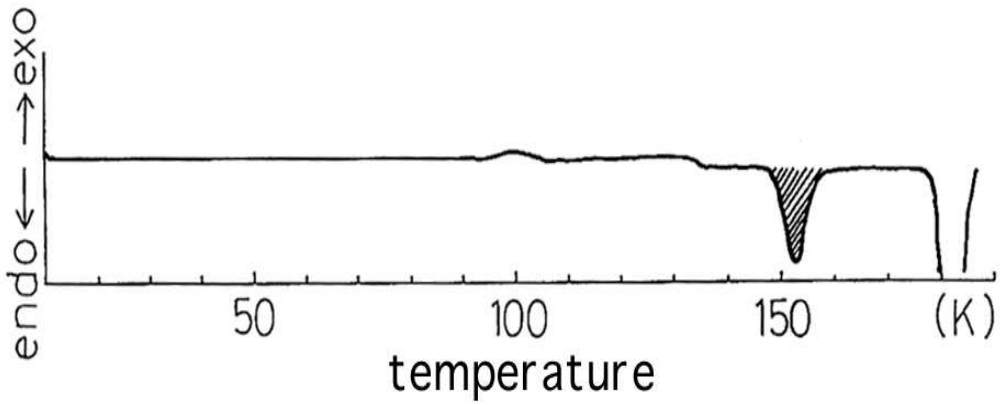

Figure 12: Same as in Fig. 10 but for H_2O ice containing 10% of CO_2. The y axis is of an arbitrary scale. The peak at 145 K is reversed to that of Fig. 10 indicating that crystallization of H_2O ice containing 10% of CO_2 is an endothermic process. The negative peak at 50 K corresponds to desorption of CO. The sublimation energy of CO at crystallization of amorphous H_2O ice is calculated by comparing the shaded areas in Figs. 10 and 12 (Kouchi, personal communication).

Table 1: Heat of sublimation of CO and CO_2 from amorphous H_2O ice estimated from the experiments by Kouchi (personal communication) and the surface binding energy measured by Sandford and Allamandola (1990)

species	estimated from Kouchi	Sandford and Allamandola (1990)
CO	2370 K	1740 K
CO_2	3550 K	2860 K

desorption. Bar-Nun et al. (1985), on the other hand, observed ejection of small grains ($\sim 1\,\mu$m) in crystallization of amorphous H_2O ice containing various kinds of molecular species, suggesting that evolving of CO from amorphous H_2O ice is an explosive process rather than simple desorption from the surface of amorphous H_2O ice. The use of binding energy of CO measured by Sandford and Allamandola (1990) as the sublimation heat is not appropriate since it can be shown that the CO binding energy is too small to account for the endothermicity seen in Fig. 11. Accordingly, we adopt heats of sublimation estimated from Kouchi's data in the following numerical calculations.

3 Evolution of icy planetesimals

We shall calculate the evolution of icy planetesimals on the basis of the results obtained in the previous sections. The basic equations that govern the evolution are presented followed by the results of the numerical calculations.

3.1 Basic equations

The evolution of icy planetesimals is described by three basic equations: 1) the heat conduction equation, 2) the diffusion equation of volatile molecules, and 3) the equation of tensile stress distribution. Equations 1) and 2) are coupled through source terms. The tensile stress distribution 3) is calculated with the solutions of Eqs. 1) and 2).

3.1.1 Heat conduction equation

We take into account of four effects in heat conduction including: 1) heat transported by advection of volatile molecules evolved to the pores, 2) the radiogenic heating whose rate is denoted by $q_{\rm rad}$, 3) heating due to latent heat deposition by crystallization of amorphous H_2O ice with the heating rate of $q_{\rm lat}$, and 4) cooling (or heating) due to sublimation (or re-condensation) of volatile molecules from (onto) the surfaces of the dust grains with the rate $q_{\rm sub}$.

For a spherically symmetric planetesimal, the temperature T at distance r from the center of the planetesimal at time t is determined by the equation of heat conduction given by

$$\rho c_{\rm p} \frac{\partial T}{\partial t} = \frac{1}{r^2}\frac{\partial}{\partial r}\left(\kappa_{\rm agg} r^2 \frac{\partial T}{\partial r}\right) + kj\frac{\partial T}{\partial r} + q_{\rm rad} + q_{\rm lat} + q_{\rm sub}, \tag{39}$$

where k is the Boltzmann constant, $c_{\rm p}$ is specific heat per unit mass of the planetesimal, and ρ is the density of the icy planetesimal given by Eq. (23).

The boundary conditions are given by

$$\left.\frac{\partial T}{\partial r}\right|_{r=0} = 0 \tag{40}$$

at the center $r = 0$ of the planetesimal, and

$$T|_{r=R} = T_0 \tag{41}$$

at the surface $r = R$. Precisely, the boundary condition at $r = R$ should be the flux boundary condition describing the energy balance among solar radiation, thermal emission from the surface of the planetesimal, and heat flow from the interior of the planetesimal. However, we took the boundary condition (41), which has been shown to little affect the results (Haruyama et al. 1993).

The specific heat $c_{\rm p}$ of a dust particle with the core mass fraction x is expressed by

$$\begin{aligned} c_{\rm p} &= x c_{\rm core} + (1-x) c_{\rm H_2O} \\ &= 8.9 \times 10^4 (1 - 0.72x) T \text{ erg g}^{-1} \text{ K}^{-1} \equiv c_{\rm p0} T, \end{aligned} \tag{42}$$

where c_{H_2O} and c_{core} are given by Haruyama et al. (1993).

In the advection term in Eq. (39), j is the flux of the volatile molecules through the pore in the planetesimal. We have approximated j to be the flux through a capillary of radius r_p, which is on the order of the size of the pore and is taken to be the radius of the dust particle a. Then the flux j is given (Prialnik and Podollak 1995) by

$$\begin{aligned} j &= \sum_i (j_{ei} + j_{si}) \\ &= -\sum_i \frac{8 r_p \pi (1-\phi)}{3\sqrt{2\pi m_i k}} \frac{d}{dr} \frac{P_i}{\sqrt{T}} - \sum_i \frac{3\pi r_p^2 (1-\phi)\sigma_i P_i}{32 kT \sqrt{2\pi m_i kT}} \frac{dP_i}{dr}, \end{aligned} \tag{43}$$

where i denotes the i-th species of the volatile molecules (i.e. CO or CO_2). σ_i denotes the geometrical cross section and m_i is mass of a molecule of i-th species. Equation of state $P_i = n_i kT$ of an ideal gas is used for the volatile molecule in the pore, where n_i is the number density of the i-th molecules in the pore. We have neglected the flux of H_2O vapor since its vapor pressure of is sufficiently low and H_2O vapor does not contribute to the heat transport at the relevant temperatures. j_{ei} and j_{si} denote the fluxes in the Epstein regime ($\lambda > r_p$, where λ is the mean free path of the volatile molecules) and in the Stokes regime ($\lambda < r_p$), respectively. Here the dependence of j on λ is given simply by the sum of the fluxes in both regimes. This simplification does not much affect the results since $\lambda > r_p$ is always realized in the course of the evolution.

The phenomenological expression of rate equation of crystallization of amorphous H_2O ice is given (Haruyama et al. 1993, see also Kouchi et al. 1994) by

$$\frac{\partial \xi}{\partial t} = \frac{1-\xi}{A} \exp\left(-\frac{E_c}{T}\right), \tag{44}$$

where ξ is the crystallization degree, E_c is activation energy of crystallization of amorphous H_2O ice in Kelvin, and A is a parameter determined from the experiments, and is on the order of the lattice vibrational period. Here we take $A = 9.54 \times 10^{-14}$ s and $E_c = 5370\,\mathrm{K}$ (Schmitt et al. 1989). It is assumed that H_2O ice in the icy mantle is initially amorphous ($\xi(t=0) = 0$). The heating rate q_{lat} due to crystallization of amorphous H_2O ice containing the volatile molecules is expressed by

$$q_{lat}(t) = \rho(1-x) L \frac{\partial \xi}{\partial t}, \tag{45}$$

where L is the *apparent* latent heat per unit mass of the ice discussed in §2.3.2, and is given by

$$\rho_{H_2O} L = H_{H_2O} n_{0,H_2O} - H_{CO} n_{0,CO} - H_{CO_2} n_{0,CO_2}, \tag{46}$$

where $n_{0,i}$ is the initial number density of the i-th species of the volatile molecules in the icy mantle. $H_{H_2O} = 185\,\mathrm{K}$ (Ghormly 1968) is the latent heat of crystallization of amorphous H_2O ice, and H_{CO} and H_{CO_2} are sublimation heats of CO and CO_2 from amorphous H_2O ice (see Table 1). For the evaluation of the absolute values of n_{0,H_2O}, $n_{0,CO}$ and n_{0,CO_2}, we assume that CO and CO_2 molecules replace H_2O molecules when they are included in H_2O ice without changing the density of H_2O ice much. Then we have

$$n_{0,H_2O} + n_{0,CO} + n_{0,CO_2} \simeq \frac{1}{\Omega_{H_2O}}, \tag{47}$$

Table 2: The values of physical quantities relevant to radiogenic heating

nuclide	λ $(\mathrm{yr}^{-1})^{1)}$	H $(\mathrm{erg\,g}^{-1})^{1)}$	$X^{2)}$
^{40}K	5.54×10^{-10}	1.66×10^{16}	8.30×10^{-7}
^{235}U	9.85×10^{-10}	1.86×10^{16}	5.10×10^{-8}
^{238}U	1.55×10^{-10}	1.83×10^{17}	1.63×10^{-8}
^{232}Th	4.95×10^{-11}	1.68×10^{17}	3.69×10^{-8}

1) From Anders and Grevesse (1989) The values are relative to unit mass of C1 chondrite.

2) From Handbook of Physical Properties of Rocks (1984)

where $\Omega_{\mathrm{H_2O}}$ is the molecular volume of H_2O. Equation (47) is valid for $n_{0,\mathrm{CO}}$, $n_{0,\mathrm{CO_2}} \ll n_{0,\mathrm{H_2O}}$.

In radiogenic heating, we take ^{40}K, ^{235}U, ^{238}U and ^{232}Th contained in the silicate core of the dust grains. The rate q_{rad} of radiogenic heating by decay of the i-th radiogenic nuclide having decay constant λ_i with mass fraction X_i is expressed by

$$q_{\mathrm{rad}}(t) = \sum_i \rho x \lambda_i H_i X_i \exp(-\lambda_i t), \tag{48}$$

where H_i is the amount of energy released per unit mass of the i-th nuclide. The abundance X_i is assumed to be chondritic. The values of the physical quantities relevant to radiogenic heating are summarized in Table 2.

The heating rate q_{sub} (i =CO or CO_2) due to re-condensation of the volatile molecules of the i-th species, whose vapor pressue is $P_{\mathrm{e},i}$, onto the surface of the icy mantle is expressed by

$$q_{\mathrm{sub}} = \sum_i \frac{3\phi H_{\mathrm{p},i}}{a} \frac{P_{\mathrm{e},i}(T) - P_i}{\sqrt{2\pi m_i k T}}, \tag{49}$$

where $H_{\mathrm{p},i}$ is the heat of condensation of *pure* CO and CO_2 since it is expected that CO and CO_2 exist as pure ices after re-condensation onto the surfaces of the dust grains. We take $H_{\mathrm{p,CO}} = 989\mathrm{K}$ (Clayton and Giauque 1932) and $H_{\mathrm{p,CO_2}} = 3057\mathrm{K}$ (Smith 1929). The vapor pressures of CO and CO_2 are taken from Yamamoto et al. (1983) as

$$\log P_{\mathrm{e,CO}}/\mathrm{dyn\,cm}^{-2} = 11.468 - 426.3/T \tag{50}$$

$$\log P_{\mathrm{e,CO_2}}/\mathrm{dyn\,cm}^{-2} = 13.033 - 1367.3/T. \tag{51}$$

3.1.2 Diffusion equation of volatile molecules

The second basic equation is the diffusion equation of volatile molecules in the planetesimal. We take into account of two source terms: 1) the evolving rate $h_{\mathrm{cry},i}$ of the volatile molecules of the i-th species from the icy mantle due to crystallization of amorphous H_2O ice, and 2) the rate $h_{\mathrm{con},i}$ of re-condensation of the molecules of the i-th species released by the process 1) onto the surface of the icy mantle.

For a spherically symmetric planetesimal, the number density n_i of the molecule of the i-th species (i =CO or CO_2) at distance r from the center of the planetesimal at time t is determined by the diffusion equation given by

$$\frac{\partial n_i}{\partial t} = -\frac{1}{r^2}\frac{\partial}{\partial r}(r^2 j_i) + h_{\mathrm{cry},i} + h_{\mathrm{con},i}, \tag{52}$$

where the flux j_i of the molecular species of i is given in Eq. (43). The boundary conditions are given by

$$\begin{aligned} \left.\frac{\partial n_i}{\partial r}\right|_{r=0} &= 0, \\ n_i|_{r=R} &= 0. \end{aligned} \tag{53}$$

The evolving rate of the molecule of the species i is expressed by

$$h_{\mathrm{cry},i} = \frac{\rho n_{0,i}(1-x)(1-\xi)}{\rho_{\mathrm{H_2O}} A}\exp(-E_{\mathrm{c}}/T), \tag{54}$$

with the use of Eq. (44), and the re-condensation rate $h_{\mathrm{con,i}}$ by

$$h_{\mathrm{con},i} = \frac{3\phi}{a}\frac{P_{\mathrm{e},i}(T) - P_i}{\sqrt{2\pi m_i kT}}. \tag{55}$$

3.1.3 Tensile stress distribution

The third basic equation is the tensile stress distribution in the planetesimal. There are two body forces acting in the planetesimal: 1) the pressure gradient of the volatile molecules, and 2) the self-gravity of the planetesimal. The strain $u(r)$ is determined by the hydrostatic equilibrium (Landau and Lifshitz, 1958) given by

$$\frac{E(1-\sigma)}{(1+\sigma)(1-2\sigma)}\frac{d}{dr}\left(\frac{1}{r^2}\frac{d}{dr}(r^2 u)\right) = \phi\frac{dP}{dr} + 4\pi G\rho^2 r, \tag{56}$$

where E is Young's modulus and σ is Poisson's ratio of the icy planetesimal. P is the sum of pressures by CO and CO_2 as $P = P_{\mathrm{CO}} + P_{\mathrm{CO_2}}$. Integrating Eq. (56) under the boundary conditions that

$$\begin{aligned} u(r) &< \infty \quad \text{at } r = 0 \\ \sigma_{rr} &= 0 \quad \text{at } r = R, \end{aligned} \tag{57}$$

the strain $u(r)$ is given by

$$u(r) = \frac{1}{r^2}\int_0^r \frac{(1+\sigma)(1-2\sigma)}{E(1-\sigma)}\phi P(r')r'^2 dr' + \frac{2\pi G(1+\sigma)(1-2\sigma)}{15E(1-\sigma)}\rho^2 r^3 + \frac{C}{3}r, \tag{58}$$

where the integration constant C is given by

$$C = \frac{2(1-2\sigma)^2}{E(1-\sigma)}\frac{3\phi}{R^3}\int_0^R P(r')r'^2 dr' - \frac{(3-\sigma)(1-2\sigma)}{E(1-\sigma)}\frac{2\pi G\rho^2 R^2}{5}. \tag{59}$$

The radial component of the stress tensor $\sigma_{rr}(r)$ is expressed in terms of $u(r)$ as

$$\sigma_{\rm rr}(r) = \frac{E(1-\sigma)}{(1+\sigma)(1-2\sigma)}\frac{du}{dr} + \frac{2E\sigma}{(1+\sigma)(1-2\sigma)}\frac{u}{r}. \tag{60}$$

Substituting Eq. (58) into Eq. (60), the radial stress $\sigma_{\rm rr}(r)$ is given by

$$\begin{aligned}\sigma_{\rm rr}(r) = -\frac{2\phi(1-2\sigma)}{r^3(1-\sigma)}\int_0^r P(r')r'^2dr' &+ \frac{2\phi(1-2\sigma)}{R^3(1-\sigma)}\int_0^R P(r')r'^2dr' \\ &+ \phi P(r) + \frac{2\pi G\rho^2(3-\sigma)}{15(1-\sigma)}(r^2-R^2).\end{aligned} \tag{61}$$

We set Poisson's ratio σ of the planetesimal to be zero because the planetesimal composed of grain aggregates is highly compressible. $\sigma_{\rm rr}(r)$ can be calculated from n_i and T obtained by solving Eqs. (39) and (52).

3.2 Numerical results

3.2.1 Parameter values

There are two parameters involved in the model, namely, the number densities $n_{0,\rm CO}$ of CO and $n_{0,\rm CO_2}$ of CO_2 in the icy mantle. The parameter space is surveyed covering the range of the CO and CO_2 fraction in polar ice in molecular clouds observed by the ISO satellite (see §4.1), where polar ice is the ice in which H_2O is the dominant species with CO and CO_2 as minor components. It has been found that the evolution of the icy planetesimals is classified into three types:

1) Endothermic ($L < 0$) model: Both CO and CO_2 are contained in significant amount of 10% relative to H_2O in the icy mantle.

2) Exothermic ($L > 0$) model: Both CO and CO_2 are contained in small amount of 1% of CO and 3% of CO_2.

3) No CO_2 model: Only CO of 3% is contained.

The parameter values of each model is summarized in Table3; the amount of CO and CO_2 in the endothermic model is near the maximum fraction of CO and CO_2 observed by the ISO satellite. Discussion on non-polar ice will be given in §4.1.

The initial condition is that a planetesimal has a uniform temperature $T_0 = 60\,\rm K$, which corresponds to the temperature at the heliocentric distance of 20 AU. We take the planetesimal radius $R = 15\,\rm km$ and the silicate mass fraction $x = 0.5$ as representative values. The essential feature of the evolution does not change between $R = 10\,\rm m$ and $R = 1000\,\rm km$.

The results depend on the initial temperature of the planetesimals and the activation energy of the surface diffusion of H_2O molecules. For comparison, we shall discuss the cases of $T_0 = 30\,\rm K$ and of the activation energy $E_{\rm s,B}(H_2O)$ measured by Berland et al. (1995) lower than $E_{\rm s,SA}(H_2O)$ by Sandford and Allamandola (1990) taken here.

Table 3: The model parameters

model	CO (%)	CO_2 (%)
endothermic model		
L <0	10	10
exothermic model		
L >0	1	3
no CO_2 model		
L >0	3	0

3.2.2 Endothermic model

temperature evolution Figure 13 shows time variation of the temperature in the planetesimal in the endothermic model at $r/R = 0$, 0.5 and 0.95. The temperature evolution may be divided into three stages:

1) At the first stage the temperature T rises gradually due to radiogenic heating, and reaches 80 K when $t = 2 \times 10^7$yr. Heat conduction is negligible in the whole planetesimal except in the region just beneath the surface, because H_2O ice of the icy mantle of the grains remains amorphous ice, which has extremely low thermal conductivity as stated in §2.1.1.

2) As T reaches 80 K, crystallization of amorphous H_2O ice begins, which leads to the increase in the cooling rate because crystallization is *endothermic* in this model. At $T = 82$ K, the radiogenic heating rate and the cooling rate are balanced and the temperature is kept constant up to $t = 4 \times 10^7$yr. At the constant temperature, crystallization of amorphous H_2O ice proceeds according to Eq. (44). CO molecules evolved by crystallization diffuse outward and escape from the planetesimal without re-condensation because of the high vapor pressure of CO. CO_2 molecules evolving from the icy mantle, on the other hand, re-condense on the surfaces of the dust grains in the planetesimal because of its low vapor pressure, and migrate to the neck. Consequently the tensile strength and the thermal conductivity of the planetesimal increases. Sintering due to H_2O proceeds to only a small extent because H_2O molecules do not diffuse much on the grain surface at the relevant temperatures. When crystallization degree ξ reaches a critical degree ξ_c, the network of the crystalline ice is formed in the icy mantle and the thermal conductivity of the planetesimal abruptly increases (see Fig. 3). Note that the temperature is uniform out to $r/R = 0.95$ up to the end of this stage at $t = 4 \times 10^7$ yr.

3) At the third stage after formation of the network of the crystalline ice, the temperature of the whole planetesimal drops to the ambient temperature $T_0 = 60$ K in 10^7 yr.

It has been confirmed that little difference arises in the temperature evolutions if we take the activation energy of surface diffusion $E_{s,B}(H_2O)$ instead of $E_{s,SA}(H_2O)$ in this model.

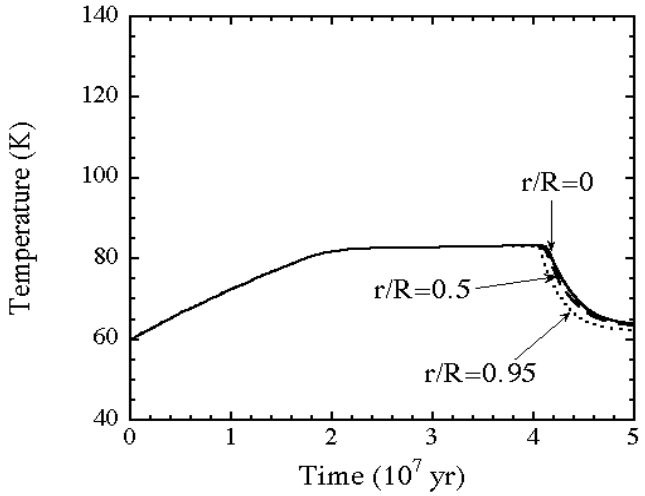

Figure 13: The temperature evolution of the icy planetesimal in the endothermic model. The solid line stands for the time variation of the temperature at $r/R = 0$, the dashed line for $r/R = 0.5$, and the dotted line for $r/R = 0.95$.

crystallization degree Figure 14 illustrates evolution of the crystallization degree in the endothermic model. No crystallization of amorphous H_2O ice occurs because of the low temperatures at the stage 1). At the stage 2), crystallization proceeds at a constant rate and ends when ξ reaches $\xi_c = 1/3$ just beneath the surface as seen in Fig. 15, which shows the final distribution of ξ. The region just beneath the surface of the planetesimal plays a role as a "stopper" of heat conduction when $\xi < \xi_c$ as follows. Cooling of the inner region of the planetesimal occurs after ξ reaches ξ_c at $r \simeq R$. The time when $\xi > \xi_c$ is realized at $r \simeq R$ is delayed for $\sim 10^6$ yr compared with that in the inner region. During the delay, crystallization proceeds up to 0.4 almost uniformly in the inner region of the planetesimal.

evolution of the chemical composition Figure 16 demonstrates evolution of the concentrations of CO and CO_2 relative to H_2O averaged over the entire region of the planetesimal. In the course of the evolution, CO and CO_2 molecules exist as vapors in the pores, as impurities in the icy mantle, and as ices on the surface of the dust grains. The total concentrations of CO and CO_2 of three kinds of the phases are plotted in Fig. 16. The concentration of CO decreases almost linearly at stage 2) with crystallization of amorphous H_2O ice. Most of the evolved CO molecules escape from the planetesimal. On the other hand, the concentration of CO_2 molecules remains constant since the vapor pressure of CO_2 is small and almost all of the evolved CO_2 molecules re-condense on the surfaces of the dust grains. The final distribution of CO and CO_2 is shown in Fig. 17. CO molecules are retained in amorphous H_2O ice, whose fraction is 60% of the total H_2O

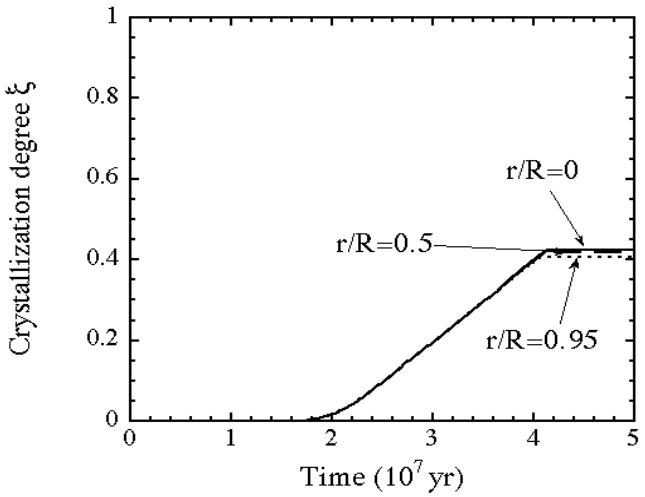

Figure 14: The evolution of the crystallization degree ξ in the endothermic model. The solid line stands for the time variation of the crystallization degree at $r/R = 0$, the dashed line for $r/R = 0.5$, and the dotted line for $r/R = 0.95$.

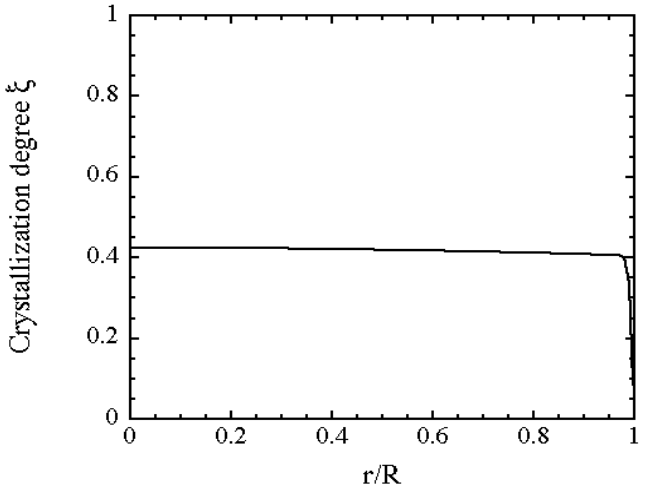

Figure 15: The final distribution of ξ of the endothermic model.

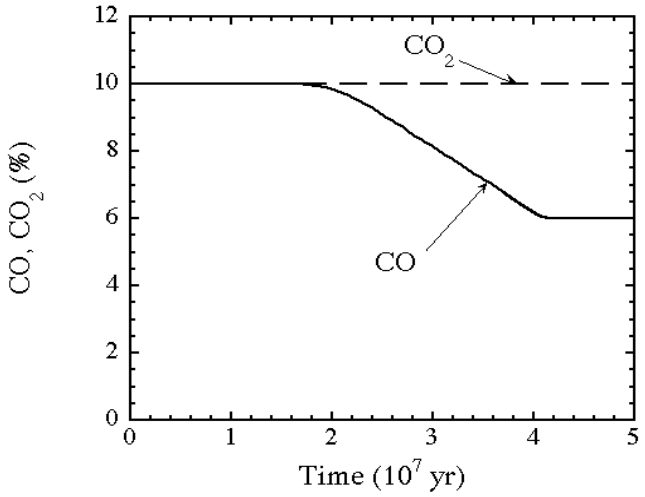

Figure 16: Evolution of the concentrations of CO (solid line) and CO_2 (dashed line) relative to H_2O averaged over the entire region of the planetesimal in the endothermic model.

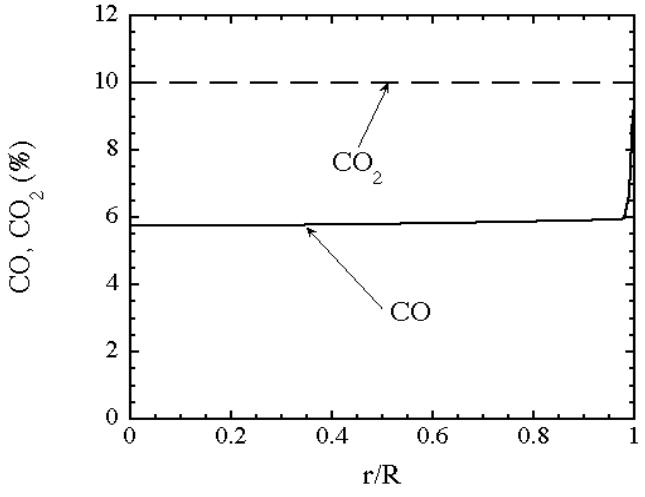

Figure 17: The distribution of CO (solid line) and CO_2 (dashed line) after evolution of the icy planetesimal in the endothermic model.

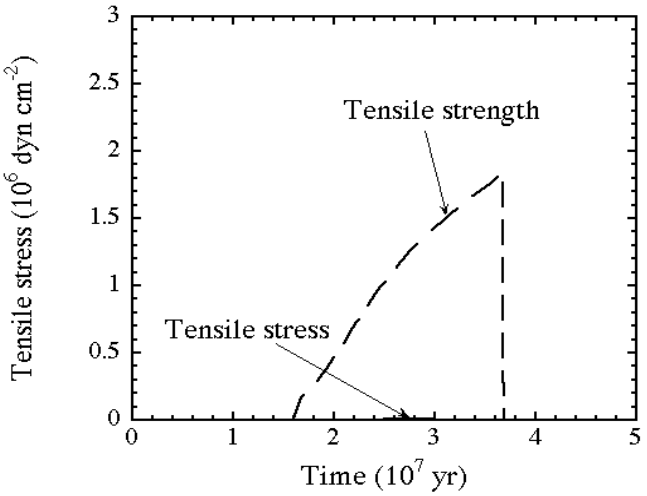

Figure 18: Evolution of the maximum tensile stress (solid line almost overlapping x axis) attained in the planetesimal in the endothermic model. The dashed line shows the tensile strength at the maximum tensile stress. Note that the maximum tensile stress is always less than the tensile strength.

ice (see Fig. 15).

tensile strength Figure 18 shows evolution of the maximum tensile stress attained in the planetesimal. The dashed line is the tensile strength at the radial distance $r_{\rm m}$ of the maximum tensile stress. During the stage 2), the tensile strength increases linearly with time by three orders of magnitude compared with the initial strength by sintering due to CO_2 and H_2O. It should be pointed out that the distance of the maximum tensile stress is kept constant at $r_{\rm m}/R \simeq 0.2$ during the stage 2). It can be seen that the maximum tensile stress due to pressure gradient of evolved CO is always less than the tensile strength, indicating that breakup of the planetesimal does not occur in the endothermic model. Toward the end of the stage 2), the volatile molecules diffuse out of the planetesimal. As a result, the tensile stress in the planetesimal interior becomes negative (compressive) by the self gravity of the planetesimal, leading to the shift of $r_{\rm m}$ toward $r = R$, where the tensile stress is zero and the tensile strength remains small. The drop of the tensile strength at $t = 3.6 \times 10^7$ yr in Fig. 18 corresponds to the shift of $r_{\rm m}$ to $r = R$.

Figure 19 shows distributions of the tensile stress and strength at the peak of the tensile stress evolution in Fig. 18. The tensile strength exceeds the tensile stress in the whole planetesimal and the breakup of the planetesimal does not occur.

Figure 20 illustrates distribution of the pressure due to the evolved CO and CO_2 molecules in the planetesimal at the same time in Fig. 19. Since the vapor pressure of CO_2 is small, the pressure plotted in Fig. 20 is mostly due to CO molecules. Note that

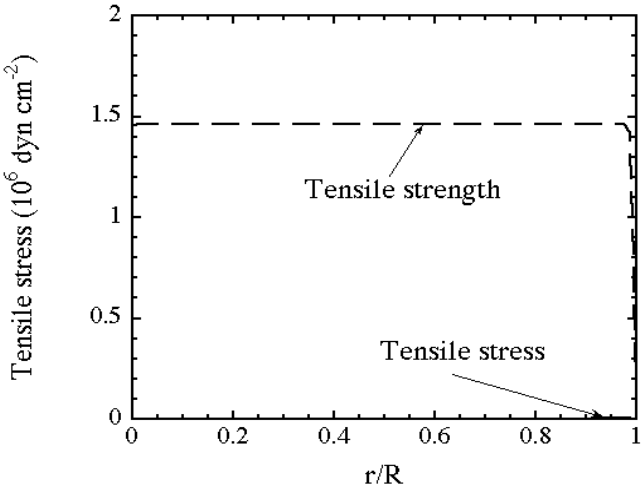

Figure 19: The tensile stress distribution at the peak of Fig. 18. The solid line (almost overlapping x axis) stands for the tensile stress distribution, and the dashed line for the distribution of the tensile strength.

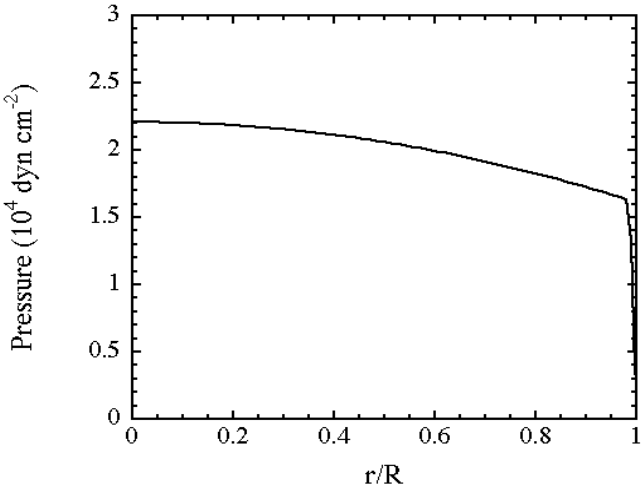

Figure 20: The pressure distribution at the peak of Fig. 18. The total pressure, which is a sum of the pressures by CO and CO_2 molecules is plotted.

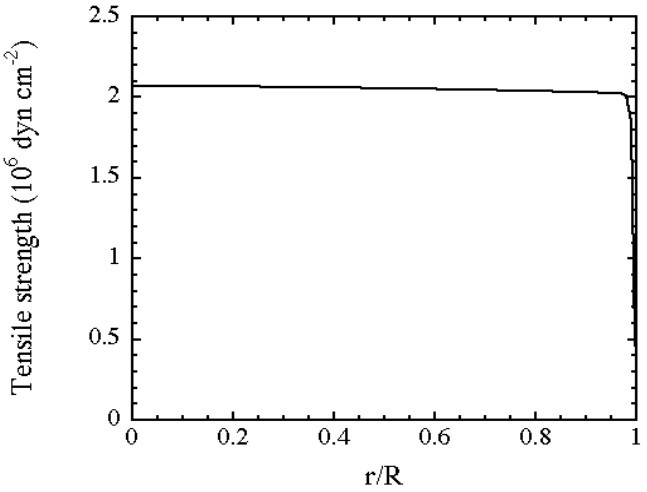

Figure 21: Distribution of the tensile strength at the end of the evolution of the icy planetesimal in the endothermic model.

the pressure ($\sim 10^4\,\mathrm{dyn\,cm^{-2}}$, the tensile stress is on the same orders of magnitude) is smaller than the tensile strength by two orders of magnitude (see Fig. 19).

There are two factors that prevents the planetesimal from breaking up: 1) The tensile strength increases from the initial value ($2.2 \times 10^3\,\mathrm{dyn\,cm^{-2}}$, §2.3.1) by three orders of magnitude because CO_2 and H_2O molecules migrate to the neck. 2) CO molecules escape outside of the planetesimal because of the long duration of stage 2) ($\sim 10^7\,\mathrm{yr}$) compared to that of the escape time scale of the vapors ($\sim 10^5\,\mathrm{yr}$).

The distribution of the tensile strength at the end of the evolution is shown in Fig. 21. It can be seen that the tensile strength after the evolution is almost uniform over the planetesimal and increased by three orders of magnitude (from $2.2 \times 10^3\,\mathrm{dyn\,cm^{-2}}$ to $2.1 \times 10^6\,\mathrm{dyn\,cm^{-2}}$).

The distribution of the normalized contact area S^* after the evolution is presented in Fig. 22. S^* is increased from 2.8×10^{-3} (see Eq. (17)) to 0.28 by sintering of H_2O and CO_2 molecules. Correspondingly, the thermal conductivity is enhanced by two orders of magnitude.

the case of $\mathbf{T_0 = 30}$K It is worth comparing the results for $T_0 = 60$K case presented in the previous sections with those for the $T_0 = 30$K case. Only the temperature evolution is shown here in Fig. 23, since almost all the results are similar. It is obvious that the essential feature of the temperature evolution is similar to that for $T_0 = 60\,\mathrm{K}$ (see Fig. 13). The difference is that the duration of the stage 1) for $T_0 = 30\,\mathrm{K}$ model is longer than that for $T_0 = 60\,\mathrm{K}$. Another difference is the cooling time of the planetesimal at the stage 3) is shorter than that for $T_0 = 60\,\mathrm{K}$. The main reason is the larger temperature gradient

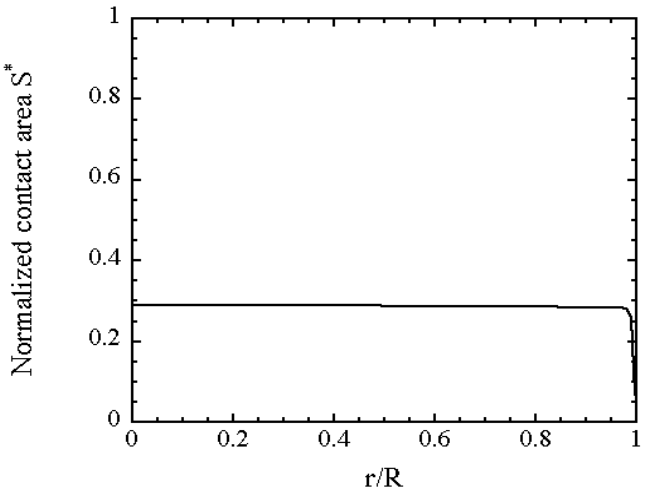

Figure 22: Distribution of the normalized contact area S^* at the end of the evolution of the icy planetesimal in the endothermic model.

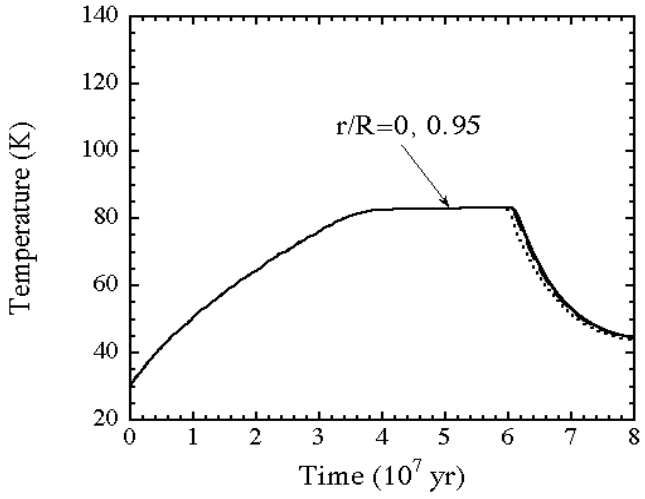

Figure 23: The temperature evolution of the endothermic model whose initial temperature is 30 K. The solid line stands for the time variation of the temperature at $r/R = 0$, the dashed line for $r/R = 0.5$, and the dotted line for $r/R = 0.95$.

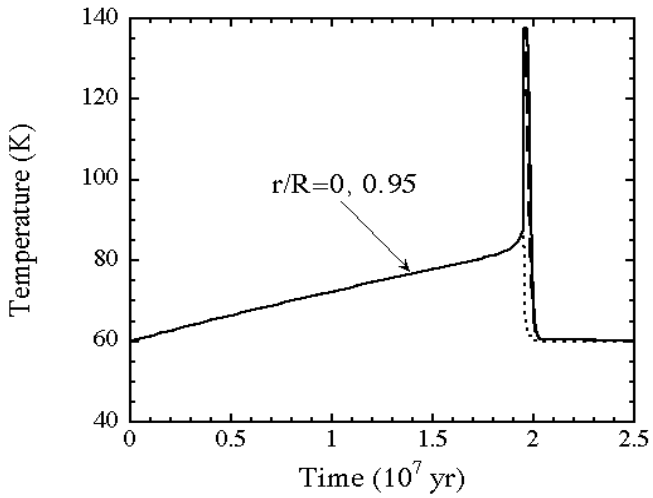

Figure 24: The temperature evolution of the icy planetesimal of the exothermic model. The solid line stands for the time variation of the temperature at $r/R = 0$, the dashed line for $r/R = 0.5$, and the dotted line for $r/R = 0.95$.

near the surface for $T_0 = 30\,\mathrm{K}$ than for $T_0 = 60\,\mathrm{K}$.

3.2.3 Exothermic model

temperature evolution Figure 24 shows the temperature evolution in the exothermic model. The temperature evolution can be divided into three stages as that in the endothermic model.

1) The first stage is the temperature increase by radiogenic heating up to $T = 80\,\mathrm{K}$ as is in the endothermic model.

2) The second is the stage of abrupt increase in the temperature at $t \simeq 2 \times 10^7\,\mathrm{yr}$. The rapid increase in T is due to release of latent heat ($L > 0$) of crystallization of amorphous H_2O ice. The temperature increase accelerates the rate of latent heat deposition due to crystallization of amorphous H_2O ice, leading to positive feedback of the temperature increase until crystallization completes. The heating rate due to latent heat deposition in crystallization overwhelms the cooling rate at this stage, although the cooling rate by heat conduction increases by five orders of magnitude when ξ exceeds ξ_c. As a result, the runaway temperature increase occurs up to the peak temperature of 140 K, and amorphous H_2O ice crystallizes completely. This is completely different behavior from that in the endothermic model. It is noted that the temperature and the crystallization degree ξ are almost uniform throughout the planetesimal until the end of this stage.

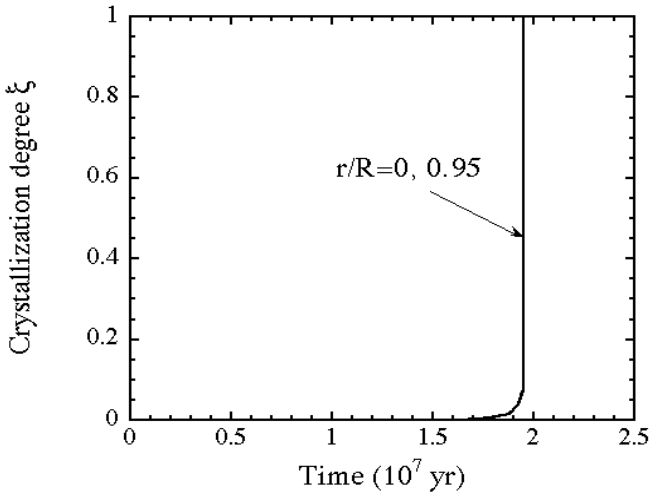

Figure 25: Evolution of the crystallization degree ξ in the exothermic model. Abrupt crystallization of amorphous H_2O ice is observed at the second stage of the temperature evolution.

3) At the third stage after complete crystallization, the temperature of the whole planetesimal drops rapidly to the ambient temperature $T_0 = 60\,\mathrm{K}$ in $t \simeq 3 \times 10^5\,\mathrm{yr}$. This cooling time-scale is shorter than that in Sirono and Yamamoto (1997) (see Fig. 3 of Appendix A) because the thermal conductivity increases by sintering of the icy mantles by surface diffusion of H_2O and CO_2.

It has been confirmed that little difference arises in the temperature evolutions if we take the activation energy of surface diffusion $E_{\mathrm{s,B}}(H_2O)$ instead of $E_{\mathrm{s,SA}}(H_2O)$ in this model.

evolution of the crystallization degree Figure 25 shows evolution of the crystallization degree ξ in the exothermic model. Complete crystallization occurs abruptly at the second stage of the temperature evolution. The final distribution of ξ is illustrated in Fig. 26. It can be seen that crystallization completes in the whole region except near the surface. Figure 26 illustrates the distribution near the surface, $0.95 \leq \xi \leq 1$. It can be seen that there is inflection in the distribution at $r/R = 0.99$. This is artifact originated from the thickness $\Delta r/R = 0.01$ used for the numerical calculations. The similar features seen in Figs. 28, 32 and 33 come from the same reason. It is necessary to take more finer grids than that used here for discussion on the surface properties such as the gas emission rate. $\Delta r/R = 0.01$ is sufficient, however, for discussion on the global distributions concerned in this thesis.

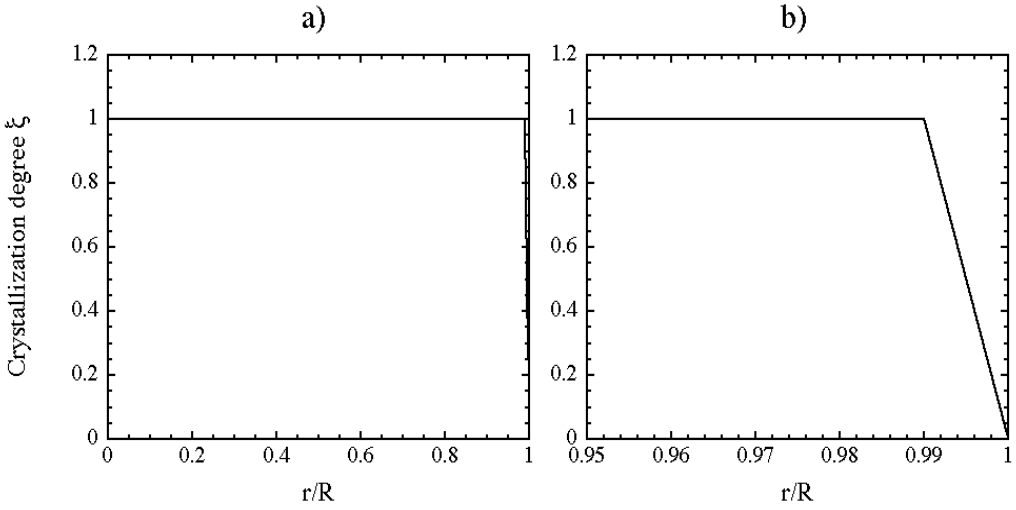

Figure 26: a) The final distribution of ξ of the whole planetesimal. b) The distribution near the surface, $0.95 \leq \xi \leq 1$. Crystallization of amorphous H_2O ice completes in the whole planetesimal except near the surface.

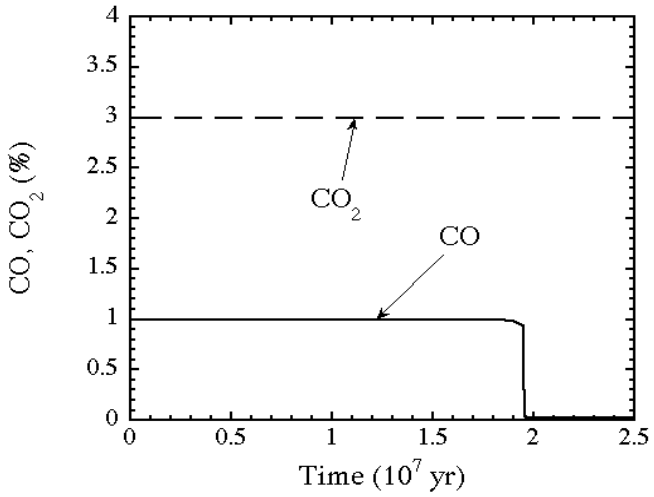

Figure 27: Evolution of average concentrations of CO (solid line) and CO_2 (dashed line) relative to H_2O in the planetesimal in the exothermic model.

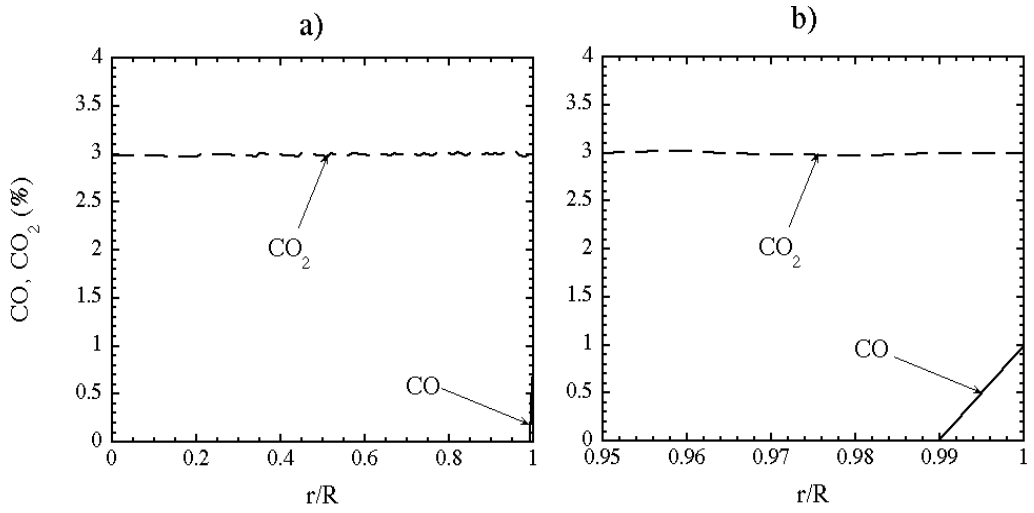

Figure 28: a) The distribution of CO (solid line) and CO_2 (dashed line) at the end of the evolution of the whole planetesimal. b) The distribution near the surface, $0.95 \leq \xi \leq 1$.

evolution of the chemical composition Figure 27 illustrates evolution of the concentrations of CO and CO_2 relative to H_2O averaged over the planetesimal in the exothermic model. The concentration of CO decreases abruptly at the second stage of the temperature evolution accompanied with runaway crystallization of amorphous H_2O ice. Only the small amount of CO molecules remains in amorphous H_2O ice near the surface of the planetesimal where temperature remains low (see Fig. 28). On the other hand, the concentration of CO_2 molecules remains constant since the vapor pressure of CO_2 is low and almost all of CO_2 molecules re-condense on the surfaces of the dust grains. The final distributions of CO and CO_2 concentration are shown in Fig. 28. Most of the CO molecules escape from the planetesimal (see Fig. 27), whereas almost all of the CO_2 molecules re-condense on the surfaces of the dust grains.

tensile stress distribution Evolution of the maximum tensile stress attained in the planetesimal is shown in Fig. 29. The dashed line in Fig. 29 is the tensile strength at the position $r_{\rm m}$ of the maximum tensile stress. At the second ($t \simeq 2 \times 10^7\,{\rm yr}$) stage of the temperature evolution, abrupt increase in both tensile stress and strength is observed. The increase in the tensile stress and strength is due to rapid pressure increase by rapid release of the volatile molecules in crystallization of amorphous H_2O ice, immediately followed by sintering of the grains due to surface diffusion of H_2O and CO_2 molecules. Note that the maximum tensile stress is always less than the tensile strength and thus breakup of the icy planetesimal does not occur in the exothermic model. As discussed in the endothermic model, the abrupt decrease in the tensile strength seen in Fig. 29 corresponds to the shift of $r_{\rm m}$ to the surface of the planetesimal, where the tensile strength remains small.

Figure 30 illustrates distributions of the tensile stress and strength at the peak ($t = 1.95 \times 10^7\,{\rm yr}$) of the evolution of the maximum tensile stress. It can be seen that the tensile

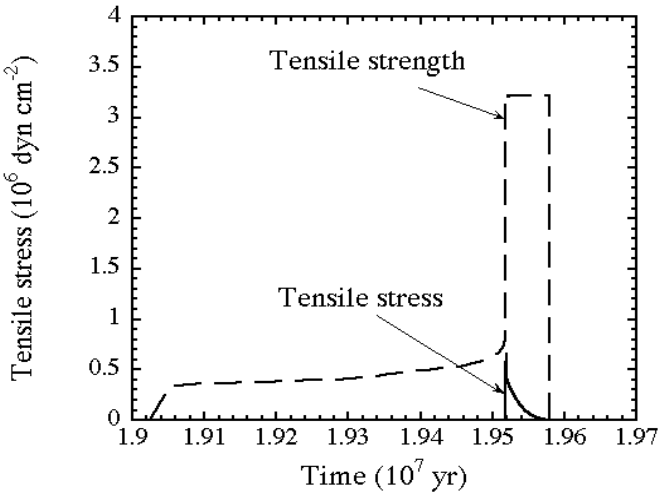

Figure 29: Evolution of the maximum tensile stress (solid line) attained in the planetesimal in the exothermic model. The dashed line shows the tensile strength at the position of the maximum tensile stress. The maximum tensile stress is always less than the tensile strength.

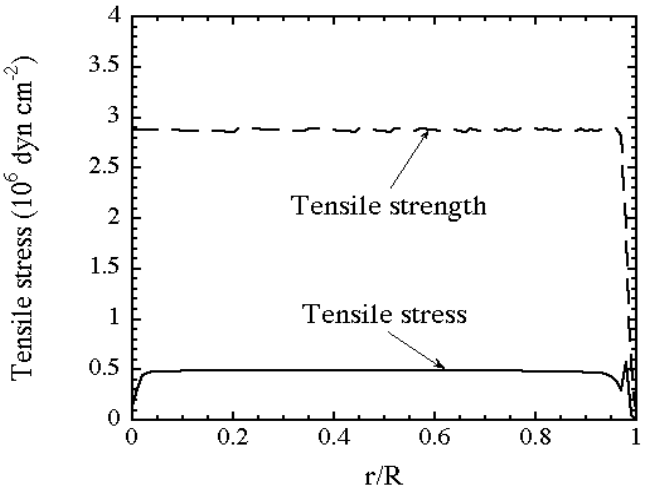

Figure 30: The tensile stress distribution at the peak of the evolution of the maximum tensile stress in Fig. 29. The solid line stands for the tensile stress distribution, and the dashed line for the distribution of the tensile strength.

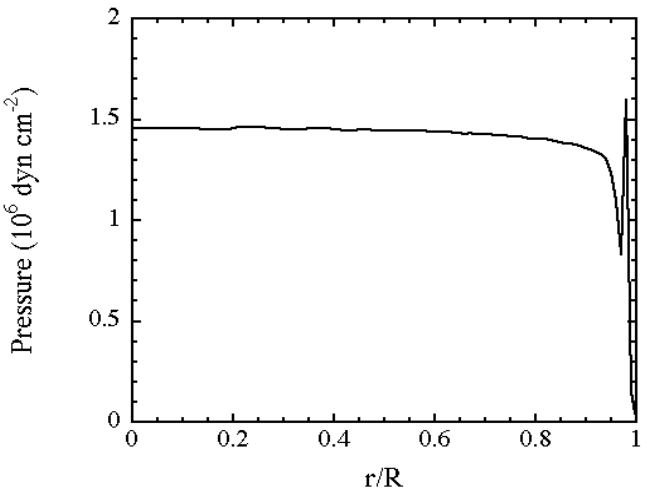

Figure 31: The pressure distribution at the peak of the evolution of the maximum tensile stress in Fig. 29. The pressure of CO and CO_2 vapors is plotted.

strength is larger than the tensile stress throughout the planetesimal. The planetesimal is not broken up in the exothermic model because the tensile strength is increased by sintering by H_2O and CO_2. The peak of the tensile stress distribution near the surface comes from abrupt release of the volatile molecules following crystallization in that region. This is because crystallization near the surface is slightly delayed ($\sim 10^5$ yr) relative to the inner region owing to the low temperature near the surface.

It is noted that the tensile stress realized in the exothermic model is larger than that in the endothermic model. This is because the crystallization time-scale at the second stage of the temperature evolution ($\sim 10^3$ yr, which is the time between 90 K and the peak temperature 140 K) in the exothermic model is shorter than the gas escape time-scale ($\sim 10^5$ yr), leading to the accumulation of CO molecules in the pore.

Figure 31 illustrates the distribution of the pressure of CO and CO_2 vapors in the planetesimal at the same time as in Fig. 30. It can be seen that the maximum pressure attained in the planetesimal is on the order of 1 atm. The peak near the surface corresponds to the delay of crystallization as seen in Fig. 30.

The distribution of the tensile strength at the end of the evolution is shown in Fig. 32. The tensile strength is almost uniform in the planetesimal and is increased by three orders of magnitude (from 2.2×10^3 dyn cm^{-2} to 3.2×10^6 dyn cm^{-2}).

The distribution of the normalized contact area S^* at the end of the evolution is presented in Fig. 33. The increased S^* by two orders of magnitude (2.8×10^{-3} to 0.37) causes rapid cooling of the planetesimal at the final stage of the temperature evolution compared to the result of Sirono and Yamamoto (1997) in which sintering is not taken into account. Although sintering occurs also in the endothermic model, the cooling time

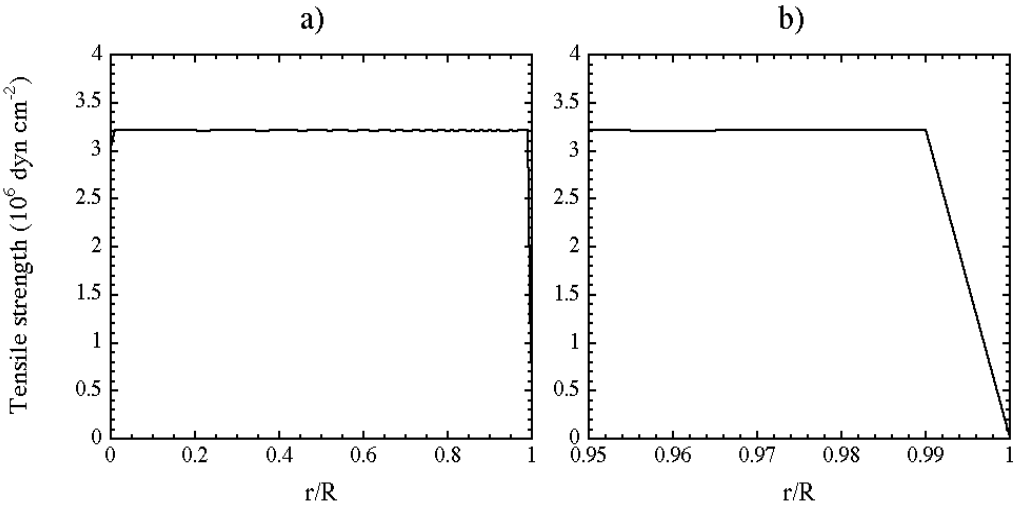

Figure 32: a) The distribution of the tensile strength of the whole planetesimal at the end of the evolution in the exothermic model. b) The distribution near the surface, $0.95 \leq \xi \leq 1$.

in the endothermic model is relatively long ($\sim 10^7$ yr) compared to that of the exothermic model ($\sim 10^5$ yr). This is because that the crystallization degree near the surface of the planetesimal in the endothermic model exceeds $\xi_c = 1/3$ only slightly.

the case of $T_0 = 30$K Temperature evolution of the planetesimal whose initial temperature is $T_0 = 30$K is shown in Fig. 34. It is obvious that the essential feature of the temperature evolution is similar to that of the case of $T_0 = 60$ K (see Fig. 24). Difference seen in Fig. 34 is that the duration of the first stage of the temperature evolution is longer than that of the case of $T_0 = 60$ K.

Other difference in the evolution is shown in Fig. 35, which shows the distributions of the CO and CO_2 concentrations relative to H_2O at the end of evolution. Although the CO_2 concentration remains constant and uniform as in $T_0 = 60$ K case, CO molecules re-condense near the surface of the planetesimal because of the low surface temperature of $T_0 = 30$ K. As a result, about 35% of CO escapes from the planetesimal, and the remaining CO is retained near the surface of the planetesimal. Occupation of pores by re-condensing CO molecules ($CO/H_2O \gg 1$ near the surface) is not observed at any CO and CO_2 concentrations surveyed in this thesis.

3.2.4 No CO_2 model

temperature evolution Figure 36 shows temperature evolution of the icy planetesimal in the no CO_2 model. The temperature evolution is essentially the same as that of the exothermic model.

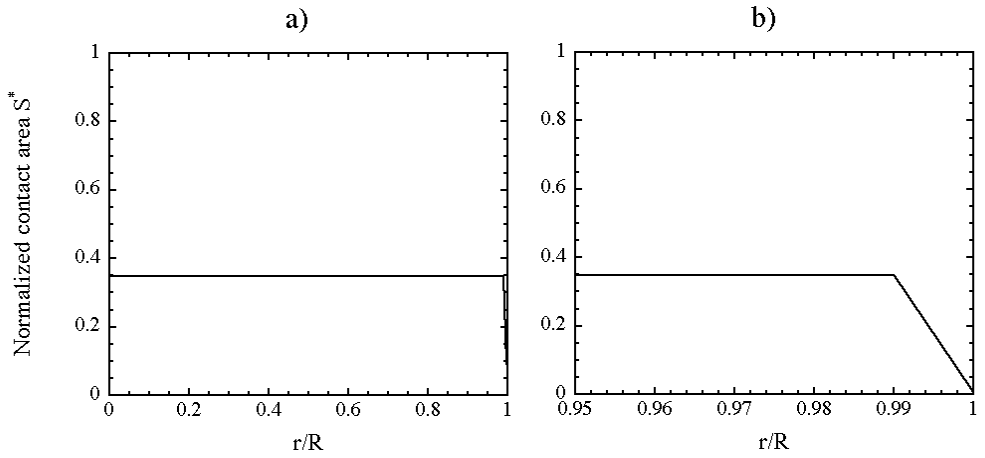

Figure 33: a) The distribution of the normalized contact area S^* of the whole planetesimal after the evolution in the exothermic model. b) The distribution near the surface, $0.95 \leq \xi \leq 1$.

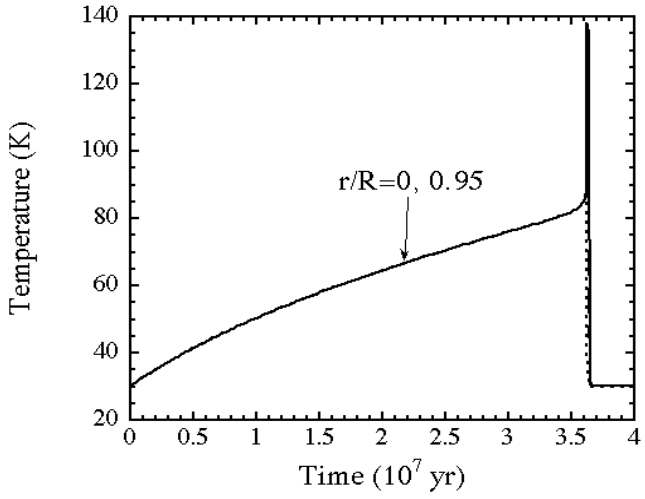

Figure 34: Temperature evolution of the planetesimal whose initial temperature is 30 K. The solid line stands for the time variation of the temperature at $r/R = 0$, the dashed line for $r/R = 0.5$, and the dotted line for $r/R = 0.95$.

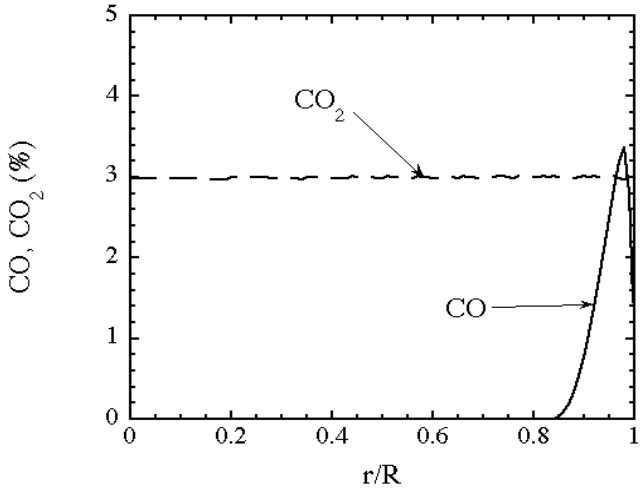

Figure 35: Distribution of the concentrations of CO (solid line) and CO_2 (dashed line) at the end of evolution. Almost all of CO_2 is retained as in the case of $T_0 = 60\,\mathrm{K}$ case. CO molecules re-condense near the surface where the temperature remains low, in contrast to the case of $T_0 = 60\,\mathrm{K}$ (see Fig. 28).

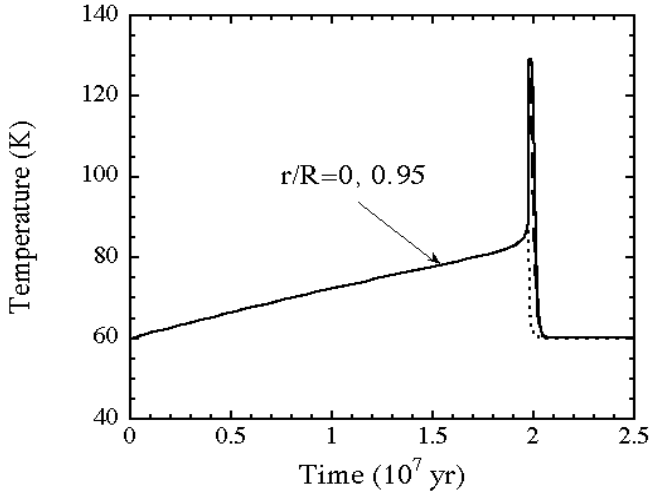

Figure 36: The temperature evolution of the icy planetesimal in the no CO_2 model. The solid line stands for the time variation of the temperature at $r/R = 0$, the dashed line for $r/R = 0.5$, and the dotted line for $r/R = 0.95$.

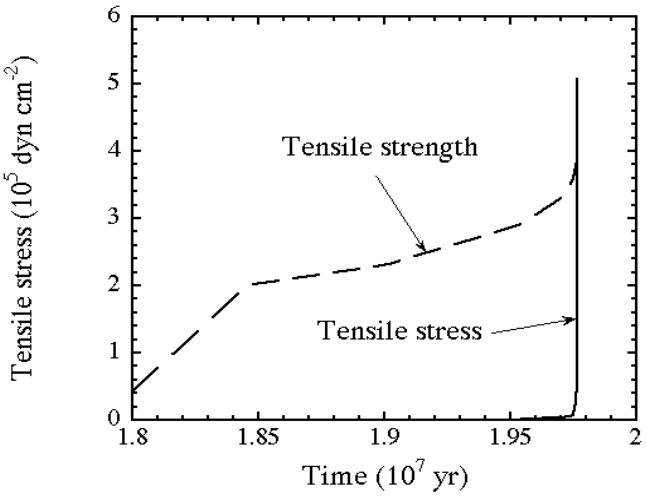

Figure 37: Evolution of the maximum tensile stress (solid line) attained in the planetesimal in the no CO_2 model. The dashed line shows evolution of the maximum tensile strength at the position of the maximum tensile stress. The maximum tensile stress exceeds the tensile strength at the second stage of the temperature evolution. $E_{\rm s,SA}(H_2O)$ is taken as the activation energy of surface diffusion of H_2O molecule.

1) The first stage is the temperature increase up to $T = 80\,{\rm K}$ by radiogenic heating, as is in the exothermic model.

2) The second is the stage of abrupt increase in the temperature at $t \simeq 2 \times 10^7\,{\rm yr}$ as is in the exothermic model. The peak temperature in this model is lower ($\simeq 130\,{\rm K}$) than that in the exothermic model ($\simeq 140\,{\rm K}$), coming from the difference in L. The evolution of the planetesimal diverges into two cases depending on the activation energy of surface diffusion of H_2O as seen in later.

3) At the third stage after the complete crystallization of amorphous H_2O ice, the temperature of the whole planetesimal drops rapidly to the ambient temperature of $T_0 = 60\,{\rm K}$ in $t = 3 \times 10^5\,{\rm yr}$.

It has been confirmed that little difference arises in the temperature evolutions if we take the activation energy of surface diffusion $E_{\rm s,B}(H_2O)$ instead of $E_{\rm s,SA}(H_2O)$ in this model. However, there is a significant difference in the evolution of tensile stress distribution as seen later.

breakup of a planetesimal Figure 37 shows evolution of the maximum tensile stress attained in the planetesimal and the tensile strength at the position of the maximum tensile stress. $E_{\rm s,SA}(H_2O)$ is taken as the activation energy of surface diffusion of H_2O molecule. It can be seen that the maximum tensile stress increases abruptly at the second

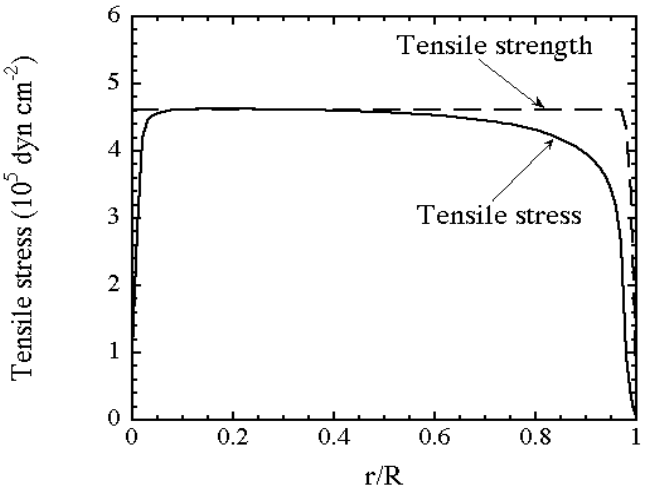

Figure 38: The distribution of the tensile stress (solid line) when breakup of the planetesimal occurs. The tensile stress exceeds the tensile strength (dashed line) at $r/R = 0.2$.

stage of the temperature evolution and reaches the tensile strength, leading to breakup of the planetesimal. The increase in the tensile strength in Fig. 37 is due to sintering by H_2O alone since there is no CO_2 molecule in this model. Figure 38 shows the tensile stress distribution at breakup of the planetesimal occurs. The breakup begins in the inner part of $r/R = 0.2$ in the planetesimal.

On the other hand, Fig. 39 shows the evolution of the tensile stress for the small activation energy of surface diffusion $E_{\rm s,B}(H_2O)$, which is smaller than $E_{\rm s,SA}(H_2O)$ by about 1000 K (cf. §2.3.3). Breakup of the planetesimal does not take place in this case. This is because that sintering by H_2O proceeds at relatively lower temperature compared to the case of $E_{\rm s,SA}(H_2O)$. As a result, the tensile strength increases rapidly and is always larger than the tensile stress even at the second stage of the temperature evolution in contrast to the case of $E_{\rm s,SA}(H_2O)$.

As we have seen above, the evolution of the icy planetesimal strongly depends on the activation energy of the surface diffusion of H_2O. The precise measurement of the activation energy is most desirable.

3.3 Summary of the evolution

For the following discussion, it is convenient to define the effective latent heat $L_{\rm eff}$ of crystallization as

$$\rho_{H_2O} L_{\rm eff} = H_{H_2O} n_{0,H_2O} - H_{CO} n_{0,CO} - (H_{CO_2} - H_{p,CO_2}) n_{0,CO_2}. \quad (62)$$

The difference between Eqs. (46) and (62) is addition of the condensation heat $H_{\rm p,CO_2}$

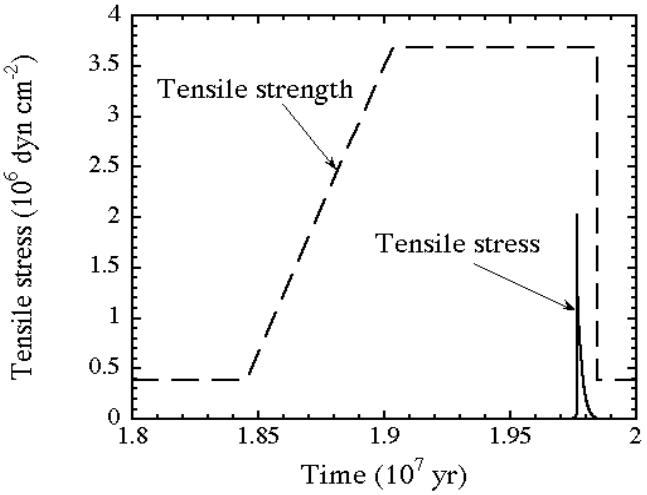

Figure 39: The same as Fig. 37, but for the small activation energy of the surface diffusion of H_2O of $E_{s,B}(H_2O)$. The tensile strength (dashed line) is always larger than the maximum tensile stress (sold line) even at the second stage in contrast to the $E_{s,SA}(H_2O)$ case (see Fig. 37).

of pure CO_2. Since CO_2 molecules re-condense immediately after release from the icy mantle, the *effective* sublimation heat taken by CO_2 is $H_{CO_2} - H_{p,CO_2}$.

Figure 40 summarizes evolution of icy planetesimals as a function of the composition of the icy mantle. The CO-CO_2 concentration plane is divided into three regions.

1) The upper-right region corresponds to evolution being typical in the endothermic model. In this region, the effective latent heat of crystallization $L_{\rm eff}$ is negative, indicating that crystallization of amorphous ice is an endothermic process effectively. The peak temperature is about 80 K where the radiogenic heating rate and the cooling rate by the endothermic crystallization are balanced. In consequence, about 40% of amorphous ice crystallizes, resulting in escape of 40% of the total CO contained in the crystallized region. This fraction is slightly larger than $\xi_c = 1/3$ as discussed in §3.2.2. On the other hand, CO_2 molecules re-condense on the surfaces of the dust grains because of the low vapor pressure of CO_2. The tensile strength of the planetesimal increases by three orders of magnitude by sintering by H_2O and CO_2. Disruption of the planetesimal does not take place because of the enhanced tensile strength and of the long duration of the stage at the peak temperature relative to the escape time-scale of CO molecules.

2) Complete crystallization of amorphous ice occurs in the upper-left region because of positive $L_{\rm eff}$. Consequently, the runaway temperature increase takes place and almost all of evolved CO molecules escape from the planetesimal. In contrast, CO_2

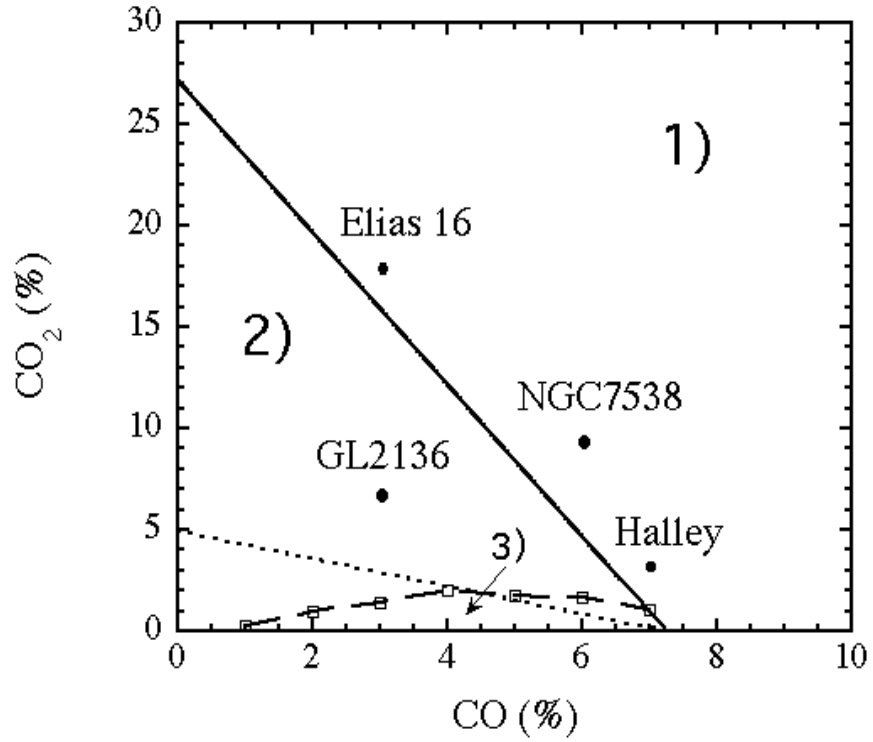

Figure 40: Summary of evolution of the icy planetesimals as a function of the concentrations of CO and CO_2. The CO-CO_2 plane is divided into three parts denoted by 1), 2) and 3), where the icy planetesimal evolves in different ways as discussed in the text. The solid line stands for $L_{\rm eff} = 0$ and dotted line for $L = 0$. The open squares connected by the dashed line are boundary between the region where disruption of the planetesimal takes place or not determined by the numerical calculations. The compositions of the ices around three embedded protostars (NGC7538, GL2136) and a background field star Elias 16 from Whittet et al. 1996 and that of Comet Halley (Mumma et al. 1993) are plotted by filled circles.

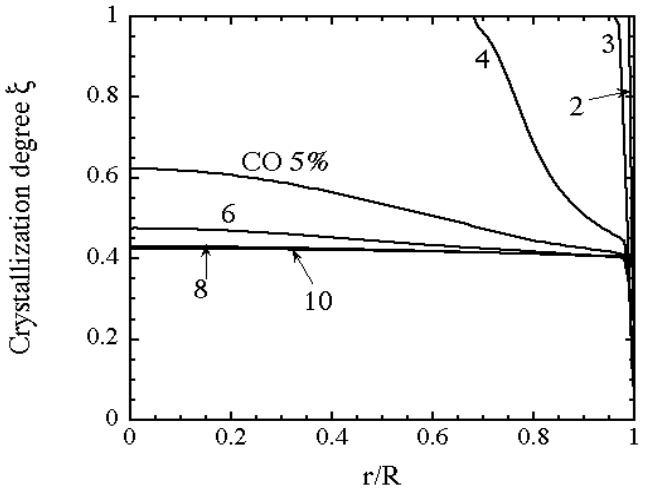

Figure 41: Distributions of ξ at the end of evolution for various $L_{\rm eff}$. $L_{\rm eff}$ is varied with the CO concentration with the CO_2 concentration being kept constant (10%). The plots correspond to 2, 3, 4, 5, 6, 8, and 10 % of CO content from the upper to the lower curve.

molecules re-condense on the the surfaces of dust grains because of its low vapor pressure. At the stage of the abrupt temperature increase, sintering by H_2O and CO_2 proceeds leading to increase in the tensile strength. The enhanced tensile strength prevents the planetesimal from being broken up, although the tensile stress due to the pressure gradient of CO vapor is larger than that in the case of 1) by two orders of magnitude.

The boundary between the regions 1) and 2) is not sharp but there is a transition region around the line defined by $L_{\rm eff} = 0$. Figure 41 shows the distributions of ξ at the end of evolution for various $L_{\rm eff}$. In Fig. 41, $L_{\rm eff}$ is varied with the CO concentration (2-10%) with the CO_2 concentration being kept constant (10%). It can be seen that the distribution of ξ gradually changes from that observed in region 1) (Fig. 15) to that of region 2) (Fig. 26). As seen in Fig. 41, crystallization proceeds from the inner region to the outer region of the planetesimal as $L_{\rm eff}$ increases (i.e. as the CO content decreases). The dotted line in Fig. 40 indicates $L = 0$ defined by Eq. (46). The region between the two lines corresponds both $L < 0$ and $L_{\rm eff} > 0$. The boundary between the regions 1) and 2) is properly defined by $L_{\rm eff} = 0$ rather than $L = 0$, because the distributions of ξ for CO concentration less than 3 % (see Fig. 41) clearly represents the distribution seen in the exothermic model as in Fig. 26.

3) There are two possibilities on the evolution of the planetesimal whose icy composition is fallen in the lower-middle region in Fig. 40. If the activation energy of

surface diffusion of H_2O is small ($E_{s,B}(H_2O)$), the evolution is similar to that in the region 2). If the activation energy is large ($E_{s,SA}(H_2O)$), on the other hand, the planetesimal is broken up by the tensile stress induced by the pressure gradient of CO vapor. Unfortunately, we cannot obtain a firm conclusion at the present study since the precise experimental value is not available.

The present thesis has firstly revealed the combined evolution of the temperature, chemical composition, the tensile stress and strength of the icy planetesimal as summarized in Fig. 40.

Table 4: Compositions of interstellar ices (from Whittet et al. 1996)

species	Elias 16	GL2136	NGC 7538
H_2O (%)	100	100	100
polar CO (%)	3	3	6*
polar CO_2 (%)	0	7	9
non-polar CO (%)	22	0	8
non-polar CO_2 (%)	0	5	6

* The abundance of CH_4 is added since the behavior of CO and CH_4 is similar.

4 Discussion

We shall discuss the implications of the results obtained in the previous sections for formation of planetary systems.

4.1 Ices in molecular clouds

The chemical compositions of ices in various molecular clouds have been measured by ISO satellite in recent years. Table 4.1 summarizes the chemical compositions of ices around embedded protostars NGC7538, GL2136 and a background field star Elias 16 (Whittet et al. 1996), showing the concentrations of CO and CO_2 in two kinds of ices, namely polar ice and non-polar ice. There are other identified species in addition to CO and CO_2 ices, CH_4, CH_3OH and XCN has been identified by ISO observations (Whittet et al. 1996). The CO content of the ice around NGC7538 shown in Table 4.1 includes the CH_4 content (2% of H_2O), since the behavior of CO and CH_4 is similar in terms of their volatilities. Note that the concentrations of the three kinds of ices are scattered in different region in Fig. 40. The results described in the previous section suggest that planetesimals formed from the ices in protoplanetary disks, if any, around the embedded protostars NGC7538, GL2136 and Elias 16 would evolve in different ways. The diversity of the planetesimal evolutions pointed out in this thesis is responsible for the emergence of the diversity of planetary systems.

The composition of the ice in Comet Halley (Mumma et al. 1993) is also plotted in Fig. 40. The initial composition of the ice forming the cometary nucleus should have had larger CO and CO_2 contents than the present contents observed, because a fraction of CO and CO_2 would have been lost in the processing in the solar nebula. Assuming that cometary nuclei are remnants of icy planetesimals whose initial composition represents the icy composition in the region of the molecular cloud from which the solar system was formed, the composition of the ice in molecular cloud forming our solar system is constrained in the region 1) in Fig. 40 and that cometary nuclei in our solar system preserve the significant amount of amorphous H_2O ice at least at the first approach to the Sun. This is consistent with the observation of the amorphous H_2O icy grains in the coma of Comet Hale-Bopp (Davies et al. 1997). If the composition of the ice forming our solar system was in the region 2), the amorphous H_2O ice should not be observed as

cometary ice.

It is worth considering the effects of non-polar ice on the evolution of the icy planetesimals. Non-polar CO_2 ice contributes to increase in the tensile strength of the planetesimal. The time-scale of sintering of CO_2, $\tau_{\rm sit,CO_2}$, by surface diffusion can be estimated from $\tau_{\rm sit,CO_2} = 2.08 \times 10^{-11} T \exp(2860/T)$ yr (see Eq. (30)), indicating that the sintering of CO_2 is sufficiently rapid for $T > 50\,{\rm K}$. Thus the planetesimal whose icy composition is in the region 3) survives the disruption by sintering of CO_2 molecules if CO_2 is contained in the planetesimal as non-polar ice. On the other hand, there is no significant effect induced by the inclusion of non-polar CO_2 ice in the planetesimals whose icy composition falls in the regions 1) and 2), just leading to further enhancement of the tensile strength by sintering by CO_2. Volatile species such as CO and CH_4 contained in non-polar ice sublime slowly and escape from the planetesimal at the stage of radiogenic heating and leave no effect on the evolution of the planetesimal.

4.2 Effects of the evolution of the tensile strength on formation of the Jovian planets

There is significant effect of increase in the tensile strength of the icy planetesimal on formation of the Jovian planets. The cores of Jovian planets are formed through mutual collisions of the icy planetesimals. According to the numerical simulations (Watanabe and Miyama 1992, Mandai et al. 1996), the larger the tensile strength of two colliding two planetesimals is, the more massive object is formed. The formation periods of the Jovian planets whose orbits are farther than that of Saturn are estimated to be longer than $\sim 10^8\,{\rm yr}$ (Matsui et al. 1997). Note that this time-scale is longer than the evolution time-scale of the icy planetesimals $\sim 10^7\,{\rm yr}$ as revealed in §3. Thus it is probable that the increase in the tensile strength affects accretion of the cores of the Jovian planets.

The condition of coalescence of two icy planetesimals of density ρ colliding with relative velocity v is roughly evaluated in terms of the tensile strength T as

$$\frac{1}{2}\rho v^2 < T, \tag{63}$$

where $v = e v_{\rm k}$ with e being the eccentricity and $v_{\rm k} = \sqrt{GM_\odot/r}$, the Keplerian velocity at the heliocentric distance r. The condition (63) is consistent with the results of SPH simulations of mutual collisions of icy planetesimals (Mandai et al. 1996). We take the values $e \simeq 10^{-3}$ (Ohtsuki et al. 1988) and $\rho = 0.5\,{\rm g\,cm^{-3}}$ (§2.2). With the initial tensile strength $T_{\rm ini} = 2.2 \times 10^3\,{\rm dyn\,cm^{-2}}$ (see §2.2.5) and the strength $T_{\rm fin} = 3.2 \times 10^6\,{\rm dyn\,cm^{-2}}$ (see Fig. 32) at the end of the evolution, we have

$$T_{\rm ini} < \frac{1}{2}\rho v^2 < T_{\rm fin} \quad \text{at } r > 3\,{\rm AU}, \tag{64}$$

implying that growth of the icy planetesimal to the cores of the Jovian planets is impossible without the increase in the tensile strength by sintering of CO_2 and H_2O.

5 Summary

This thesis has examined evolution of the temperature, chemical composition, tensile stress and strength of the icy planetesimals. It has been revealed that the evolution diverges into three paths depending on the initial chemical composition of the planetesimal as summarized in Table 5.

Table 5: Summary of evolution of the icy planetesimals

composition of ice	peak temperature	crystallization degree at the end of evolution	breakup of the planetesimal
CO, $CO_2 \sim 10\%$	80 K	40 %	No
CO, $CO_2 \sim 1\%$	140 K	100 %	No
CO$\sim 1\%$, $CO_2 \sim 0\%$	130 K	100 %	Yes*

* Depending on the surface activation energy of H_2O molecule on amorphous H_2O ice.

This thesis has clarified the combined evolution of the temperature, chemical composition, tensile stress and strength of the icy planetesimal. The results obtained in this thesis reveal the missing link between the dust grains in molecular clouds and the present objects in our solar system as follows:

1) A comparison has been carried out between the chemical compositions of the ice in the icy planetesimals categorized above and in molecular clouds and cometary nuclei. The physical processes pointed out in this thesis cause the emergence of the diversity of the planetary systems. The chemical composition of the ice, which formed our solar system icy bodies, can be constrained to be both CO and CO_2 rich.

2) The condition of growth of the planetesimal by the mutual collisions has been estimated in terms of the tensile strength. It has been pointed out that increase in the tensile strength is necessary to growth of the planetesimals to formation of the Jovian planets.

With regard to 2), it has been clearly shown that the formation processes of the Jovian planets and the materials evolution of the icy planetesimals are coupled with each other. To date, dynamical studies has assumed that the perfect inelastic collision when two planetesimals collide with each other. As revealed in this study, however, it is apparent that the materials evolution of the planetesimals must be studied simultaneously with the dynamical evolution of the swarm of planetesimals. The collisional process between planetesimals must be investigated in detail from the viewpoint of the materials science. Although collisions between dust aggregates have been investigated theoretically (Dominik and Tielens 1997) and experimentally (Blum and Munch 1993, Bridges et al. 1996), a few attempts have been made to simulate the collision between porous planetesimals (Watanabe and Miyama 1992, Mandai et al. 1996). The difficulty lies in the present status that both physical and chemical behavior of the dust aggregate on the collision

are uncertain and there is no constitutive equation of the dust aggregate based on the firm physical grounds. The peculiar properties of the granular materials (Hayakawa et al. 1995, Jaeger and Nagel 1996), which do not exhibit mechanical properties like either solid bulk materials or fluids, might affect the mechanical response of the planetesimal on the collision. Collisions between planetesimals might affect their chemical composition and strength as well.

The combined study of both dynamical and materials evolution of the swarm of planetesimals should be carried out in the near future; the study carried out in this thesis may be regarded as a milestone of the future study of the origin and the evolution of the planetary systems.

Acknowledgments

I am extremely grateful to Prof. T. Yamamoto of Hokkaido University, for helpful discussion and continuous encouragement. Appreciation is expressed to Prof. A. Kouchi for providing the data of DTA analysis of amorphous ice and for critical comments. I would like to thank Profs. T. Mukai, A. Hashimoto and M. Arakawa for their valuable comments and suggestions. I wish to express my sincere appreciation for the assistance of Mr. H. Mandai and other colleagues in Hokkaido University. This work is supported by JSPS.

References

[1] Anders, E. and Grevesse, N. 1989. Abundances of the elements. *Geochim. Cosmochim. Acta.*, **53**, 197-214.

[2] Bar-Nun, A., Herman, G., Laufer, D. and Rappaport, M. L. 1985. Trapping and release of gases by water ice and implications for icy bodies. *Icarus*, **63**, 317-332.

[3] Berland, B. S., Brown, D. E., Tolbert, M. A., and George, S. M. 1995. Refractive index and density of vapor-deposited ice. *Geophys. Res. Lett.*, **22**, 3493-3496.

[4] Blum, J. and Munch, M. 1993. Experimental investigations on aggregate-aggregate collisions in the early solar nebula. *Icarus*, **106**, 151-167.

[5] Bridges, F. G., Supulver, K. D., Lin, D. N. C., Knight, R. and Zafra, M. 1996. Energy loss and sticking mechanisms in particle aggregation in planetesimal formation. *Icarus*, **123**, 422-435.

[6] Brown, R. H., Cruikshank, D. P., Pendleton, Y. and Veeder, G. J. 1997. Surface composition of Kuiper belt object 1993SC. *Science*, **276**, 937-939.

[7] Capria, M. T., Capaccioni, F., Coradini, A., De Sanctis, M. C., Espinasse, S., Federico, C., Orosei, R. and Salomone, M. 1996. A P/Wirtanen evolution model. *Planet. Space. Sci.*, **44**, 987-1000.

[8] Chiar, J. E., Adamson, A. J., Kerr, T. H. and Whittet, D. C. B. 1995. High-resolution studies of solid CO in the taurus dark cloud: Characterizing the ices in quiescent clouds. *Astrophys. J.*, **455**, 234-243.

[9] Chiar, J. E., Adamson, A. J. and Whittet, D. C. B. 1996. Three micron hydrocarbon and methanol absorption in taurus. *Astrophys. J.* **472**, 665-672.

[10] Chokshi, A., Tielens, A. G. G. M. and Hollenbach, D. 1993. Dust coagulation. *Astrophys. J.*, **407**, 806-819.

[11] Clayton, J. O. and Giauque, W. F. 1932. The heat capacity and entropy of carbon monoxide. Heat of vaporization. Vapor pressures of solid and liquid. Free energy to 5000 K from spectroscopic data. *J. Am. Chem. Soc.*, **54**, 2610-2626.

[12] Crovisier, J., Leech, K., Bockelee-Morvan, D., Brooke, T. Y., Hannar, M. S., Altieri, B., Keller, H. U. and Lellouch, E. 1997. The spectrum of Comet Hale-Bopp (C/1995 O1) observed with the Infrared Space Observatory at 2.9 astronomical units from the Sun. *Science*, **275**, 1904-1907.

[13] Davies, J.K., Roush, T.L., Cruikshank, D.P., Bartholomew, M.J., Geballe, T.R., Owen, T. and De Bergh, C. 1997. The detection of water ice in Comet Hale-Bopp. *Icarus*, **127**, 238-245.

[14] Dominik, C., and A. G. G. M. Tielens 1997. The physics of dust coagulation and the structure of dust aggregates in space. *Astrophys. J.*, **480**, 647- 673.

[15] Espinasse, S., Klinger, J., Ritz, C. and Schmitt, B. 1991. Modeling of the thermal behavior and of the chemical differentiation of cometary nuclei. *Icarus*, **92**, 350-365.

[16] Ghormley, J. A. 1968. Enthalpy change and heat-capacity changes in the transformation from high-surface-area amorphous ice to stable hexagonal ice, *J. Chem. Phys.*, **48**, 503-508.

[17] Gold, L. W. 1958. Some observations on the dependence of strain on stress in ice. *Can. J. Phys.*, **36**, 1265-1275.

[18] Greenberg, J. M. 1982. What are comets made of? A model based on interstellar dust, in *Comets*, edited by L. L. Wilkening, Univ. Arizona Press, Tucson, pp. 131-163.

[19] Greenberg, J. M., Zhao, N. S. and Hage, J. I. 1989. The interstellar dust model of comet dust constrained by 3.4 μm and 10 μm emission. *Adv. Space. Res.*, **9**(3), 3 -11.

[20] Greenberg, J. M., Mizutani, H. and Yamamoto T. 1995. A new derivation of the tensile strength of cometary nuclei: application to Comet Shoemaker-Levy 9. *Aston. Astrophys. (Lett.)*, **295**, L35-L38.

[21] Handbook of Chemistry and Physics, 62nd ed, edited by R. C. Weast, and M. J. Astle, *CRC Press, Inc, Boca Raton,* Florida, 1981.

[22] Handbook of Physical Properties of Rocks, vol.3, edited by S. C. Robert, *CRC Press, Inc, Boca Raton,* Florida, 1984.

[23] Haruyama, J., Yamamoto, T., Mizutani, H. and Greenberg, J. M. 1993. Thermal history of comets during residence in the Oort cloud: effect of radiogenic heating in combination with the very low thermal conductivity of amorphous ice. *J. Geophys. Res.*, **98 E8**, 15079-15090.

[24] Hashin, Z. and Shtrikman, S. 1962. A variational approach to the theory of the effective magnetic permeability of multiphase materials. *J. Appl. Phys.*, **33**, 3125-3131.

[25] Hayakawa, H., Nishimori, H., Sasa, S. and Taguchi, Y.-H. 1995. Dynamics of granular matter. *Jpn. J. Appl. Phys.*, **34**, 397-408.

[26] Hayashi, C., Nakazawa, K. and Nakagawa, Y. 1985. Formation of the solar system. In *Protostars and Planets II*, (eds. D. C. Black and M. S. Matthews), pp. 1100-1153. Univ. Arizona Press, Tuscon.

[27] Hobbs, P. V. 1974. *Ice Physics*, Clarendon Press, Oxford.

[28] Horai, K. and Susaki, J. 1989. The effect of pressure on the thermal conductivity of silicate rocks up to 12 kbar. *Phys. Earth. Planet. Inter.*, **55** 292-305.

[29] Jacobs, D. J., and M. F. Thorpe 1996. Generic rigidity percolation in two dimensions. *Phys. Rev. E*, **53**, 3682-3693.

[30] Jaeger, H. M. and Nagel, S. R. 1996. Granular solids, liquids, and gases. *Rev. Mod. Phys.*, **68**, 1259-1273.

[31] Johnson, K. L. 1985. *Contact mechanics*, Cambridge Univ. Press, Cambridge.

[32] Jewitt, D. and Luu, J. 1997. Optical-infrared spectral diversity in the Kuiper belt. preprint.

[33] Kessler, M. F., Steinz, J. A., Anderegg, M.E., Clavel, J., Drechsel, G., Estaria, P., Faelker, J., Riedinger, J.R., Robson, A., Taylor, B.G. and Ximenez de Ferran, S. 1996. The infrared space observatory (ISO) mission. *Astron. Astrophys.*, **315**, L27-31.

[34] Kirkpatrick, S. 1973. Percolation and conduction. *Rev. Mod. Phys.*, **45**, 574-588.

[35] Kouchi, A. Evaporation of H_2O-CO_2 ice and its astrophysical implications. *J. Cryst. Growth*, **99**, 1220-1226, 1990.

[36] Kouchi, A., Greenberg, J. M., Yamamoto, T. and Mukai, T. 1992. Extremely low thermal conductivity of amorphous ice: relevance to comet evolution. *Astrophys. J.*, **388**, L73-L76.

[37] Kouchi, A., Yamamoto, T., Kozasa, T., Kuroda, T. and Greenberg, J.M. 1994. Conditions for condensation and preservation of amorphous ice and crystallinity of astrophysical ices. *Astron. Astrophys.*, **209,** 1009-1018.

[38] Kuczynski, G. C. 1949. Self-diffusion in sintering of metallic particles. *Metals Transactions*, **185**, 169-178.

[39] Landau, L. D. and Lifshitz, E. M. 1958. *Theory of elasticity*, Pergamon Press, New York.

[40] Landauer, R. 1952. The electrical resistance of binary metallic mixtures. *J. Appl. Phys.*, **23**, 779-784.

[41] Luu, J and Jewitt, D. 1996. Color diversity among the Centaurs and Kuiper Belt objects. *Astron. J.*, **112**, 2310-2318.

[42] Maeno, K. and Ebinuma, T. 1983. Pressure sintering of ice and its implication to the densification of snow at polar glaciers and ice sheets. *J.Phys. Chem.*, **87**, 4103-4110.

[43] Mandai, H., Shirono, S., Watanabe, S. and Yamamoto, T. 1996. SPH simulation of collision of planetesimal including the plastic deformation. *proc. 29th ISAS Lunar and Planetary Symposium*, pp.123-126.

[44] Matsui, T., H. Nagahara, A. Fujiwara, S. Watanabe, S. Ida, Y. Abe, M. Nakamura, G. Komatsu, and T. Yamamoto 1997. *Hikaku wakusei gaku* (in Japanese), pp. 184. Iwanami-syoten, Tokyo.

[45] Mayor, M. and D. Queloz 1995. A Jupiter-mass companion to a solar-type star. *Nature*, **378**, 355-359.

[46] Maxwell, J. C. 1904. *A treatise on electricity and magnetism*, 3rd ed., The Clarendon Press, Oxford.

[47] Mumma, M. J., Weissman, P. R. and Stern, S. A. 1993. Comets and the origin of the solar system: reading the rosetta stone. In *Protostars and Planets III*, (eds. E. H. Levy and J. I. Lunine), pp. 1177-1252. Univ. Arizona Press, Tuscon.

[48] Ohtsuki, K., Nakagawa, Y. and Nakazawa, K. 1988. Growth of the Earth in nebular gas. *Icarus*, **75**, 552-565.

[49] Ohtsuki, K., Ida, S., Nakagawa, Y. and Nakazawa, K. 1993. Planetary accretion in the solar gravitational field. In *Protostars and Planets III*, (eds. E. H. Levy and J. I. Lunine), pp. 3-45. Univ. Arizona Press, Tuscon.

[50] Pearce, A. J. and Haniff, M. S. 1987. Light-scattering experiments from a carbon dioxide surface near the critical point: A data reduction procedure. *J. Colloid. Inter. Sci.*, **119**, 315-325.

[51] Prialnik, D., and Podolak, M. 1995. Radioactive heating of porous comet nuclei. *Icarus*, **117**, 420-430.

[52] Rickman, H. 1989. The nucleus of Comet Halley: Surface structure, mean density gas and dust production. *Adv. Space. Res.*, **9**(3), 59-71.

[53] Russel, H. W. 1935. Principles of heat flow in porous insulators. *J. Am. Ceram. Soc.*, **18**, 1-5.

[54] Sandford, S. A. and Allamandola, L. J. 1988. The condensation and vaporization behavior of H_2O:CO ices and implications for interstellar grains and cometary activity. *Icarus*, **76**, 201-224.

[55] Sandford, S. A. and Allamandola, L. J. 1990. The physical and infrared spectral properties of CO_2 in astrophysical ice analogs. *Astrophys. J.*, **355**, 357-372.

[56] Schmitt, B., Espinasse, S., Grim, R. A. J., Greenberg, J.M. and Klinger, J. 1989. Laboratory studies of cometary ice analogues. *ESA SP*278, pp. 613-619.

[57] Sekanina, Z. 1993. Disintegration phenomena expected during collision of Comet Shoemaker-Levy 9 with Jupiter. *Science*, **262**, 382-387.

[58] Sekiya, M. 1983. Gravitational instabilities in a dust-gas layer and formation of planetesimals in the solar nebula. *Prog. Theor. Phys.*, **69**, 1116-1130.

[59] Shu, F., Najita, J., Galli, D., Ostriker, E. and Lizano, S. 1993. The collapse of clouds and the formation and evolution of stars and disks. In *Protostars and Planets III*, (eds. E. H. Levy and J. I. Lunine), pp. 3-45. Univ. Arizona Press, Tuscon.

[60] Sirono, S. 1998. in preparation.

[61] Sirono, S. and Yamamoto, T. 1997. Thermal conductivity of granular materials relevant to the thermal evolution of cometary nucleus. *Planetary and Space Science*, **45**, 827-834.

[62] Smith, A. W. 1929. *International Critical Tables, V*, pp. 138.

[63] Stauffer, D., and Aharony, A. 1994. *The introduction to percolation theory*, 2nd ed., Taylor and Francis, Bristol.

[64] Swinkels, F. B. and Ashby, M. F. 1981. A second report on sintering diagrams. *Acta Metallurgica*, **29**, 259-281.

[65] Tielens, A. G. G. M., Tokunaga, A. T., Geballe, T. R. and Bass, F. 1991. Interstellar solid CO: Polar and nonpolar interstellar ices. *Astrophys. J.*, **381**, 181-199.

[66] Thorpe, M. F., and E. J. Garboczi 1987. Site percolation on central-force elastic networks. *Phys. Rev. B*, **35**, 8579-8586.

[67] Watanabe, S. and Miyama, S. 1992. Collision and tidal interaction between planetesimals. *Astroph. J.*, **391**, 318-335.

[68] Whittet, D. C. B., Schutte, W. A., Tielens, A. G. G. M., Boogert, A. C. A., de Graauw, Th., Ehrenfreund, P., Gerakines, P. A., Helmich, F. P., Prusti, T. and van Dishoeck, E. F. 1996. An ISO SWS view of interstellar ices–First results. *Astron. Astrophys.*, **315**, L357-360.

[69] Weidenschilling, S. J. 1997. The origin of comets in the solar nebula: A unified model. *Icarus*, **127**, 290-306.

[70] Weidenschilling, S. J. and Cuzzi, J. N. 1993. Formation of planetesimals in the solar nebula. In *Protostars and Planets III*, (eds. E. H. Levy and J. I. Lunine), pp. 1031-1060. Univ. Arizona Press, Tuscon.

[71] Wetherill, G. W. and Stewart, G. R. 1989. Accumulation of a swarm of small planetesimals. *Icarus*, **77**, 330-357.

[72] Yamamoto, T. and Kozasa, T. 1988. The cometary nucleus as an aggregate of planetesimals. *Icarus*, **75**, 540-551.

[73] Yamamoto, T., Nakagawa, N. and Fukui, Y. 1983. The chemical composition and thermal history the ice of a cometary nucleus. *Astron. Astrophys.*, **122**, 171-176.

[74] Yamamoto, T., Mizutani, H. and Kadota, A. 1994. Are 1992QB1 and 1993FW remnant planetesimals? *Publ. Astron. Soc. Japan*, **46**, L5-L9.

[75] Yeomans, D. K., Barriot, J.-P., Dunham, D. W., Farquhar, R. W., Giorgini, J. D., Helfrich, C. E., Konopliv, A. S., McAdams, J. V., Miller, J. K., Owen Jr, W. M., Scheeres, D. J., Synnott, S. P. and Williams, B. G. 1997. Estimating the mass of asteroid 253 Mathilde from Tracking Data During the NEAR flyby. *Science*, **278**, 2106-2109.